Alma Mater Studiorum Università di Bologna
Archivio istituzionale della ricerca

In–situ quantification of mechanical and permeability properties on outcrop analogues of offshore fractured and weathered crystalline basement: Examples from the Rolvsnes granodiorite, Bømlo, Norway

(Article begins on next page)

01 May 2024

1 **In–situ quantification of mechanical and permeability properties on outcrop analogues of**

2 **offshore fractured and weathered crystalline basement: Examples from the Rolvsnes**

3 **granodiorite, Bømlo, Norway**

4

5 Alberto Ceccato*, Giulio Viola*, Giulia Tartaglia, Marco Antonellini

6 * Corresponding Authors; email: alberto.ceccato@unibo.it; giulio.viola3@unibo.it

7 Dipartimento di Scienze Biologiche, Geologiche ed Ambientali – BiGeA, Alma Mater Studiorum –

8 Università di Bologna – via Zamboni, 67, 40126 Bologna, Italy

9 **Abstract**

10 Fractured and weathered crystalline basement units below erosional unconformities potentially

11 represent unconventional reservoirs for georesources (oil, mineral and water). The reservoir

12 properties and characteristics strongly depend on secondary processes connected to the local

13 structural and alteration/weathering history. Here we present the results of in–situ field quantification

14 of mechanical (uniaxial compressive strength) and petrophysical (permeability) properties of a

15 fractured and weathered crystalline basement at selected outcrops on the island of Bømlo (western

16 Norway). The Bømlo outcrops are believed to represent an onshore analogue of the unconventional

17 oil reservoir hosted in the offshore Utsira High granodioritic fractured basement (northern North Sea).

18 The off– and onshore crystalline basements have both undergone surficial weathering during the

19 Mesozoic, as shown by the occurrence of a dated, variably thick saprolitic profile on top of fresh

20 fractured basement blocks. The Bømlo crystalline basement is characterized by a complex and highly

21 permeable fracture network. Fault rocks within its fault zones are characterised by an anisotropic

22 mechanical strength and by an average permeability that is two orders of magnitude larger than that

23 of the host rock. The matrix permeability and mechanical strength are significantly affected by

24 alteration/weathering products. Analysis of the textural and mineralogical characteristics of the

25   weathered outcrops allowed us to constrain the variation of permeability and mechanical strength as

26   a function of increasing alteration and to infer their distribution in the, now eroded, top–basement

27   weathering profile on Bømlo. Weathering enhances permeability and drastically decreases the

28   mechanical strength. Nevertheless, evolved saprolitic horizons may act as low–permeability top–seal

29   units to the fractured and weathered crystalline basement reservoir. The obtained permeability and

30   mechanical data are finally used to better constrain the potential reservoir rocks, the fluid migration

31   pathways, and to discuss their role in the geomechanics of a conceptualised fractured and weathered

32   crystalline basement unconventional reservoir.

35

36

1. Introduction

Faults, fractures, and related alteration zones control fluid transport within low–permeability crystalline basement rocks at different crustal levels within all tectonic settings and geological conditions (Stober and Bucher, 2015). Indeed, brittle deformation and alteration processes may drastically affect the mechanical strength and permeability of inherently stiff, low–permeability crystalline basement rocks through the development of secondary porosity (Brace, 1984; Bruhn et al., 1994; Caine et al., 1996; Stober and Bucher, 2007; Place et al., 2016; Staněk and Géraud, 2019). A better understanding of how these processes affect the rock mechanical strength and the properties controlling fluid flow is, therefore, of interest to geoscientific research and many applied fields. Examples are the geological characterisation necessary to the construction of deep nuclear waste and CO_2 repositories (Armitage et al., 2013), the better definition of crustal rheology and rock mechanics (Caine et al., 1996; Sibson and Rowland, 2003) and the exploration and production of georesources (Dewandel et al., 2006; Stober and Bucher, 2015; Kitchka et al., 2017). Specific to this last point, in the recent past, economically viable unconventional oil plays have been defined in structural highs within fractured and weathered crystalline basement blocks (Koning, 2003; Luthi, 2005; Kitchka et al., 2017; Braathen et al., 2018; Bonter and Trice, 2019; Holdsworth et al., 2019, 2020; Trice et al., 2019; McCaffrey et al., 2020). There, the constituent elements of a reservoir include (Riber et al., 2015, 2017; Fredin et al., 2017b; Braathen et al., 2018; Lothe et al., 2018; Walter et al., 2018; McCaffrey et al., 2020): (1) the host crystalline rock, characterised by primary low–porosity/permeability; (2) fractures, fault zones, mineral veins and open fissures characterised by enhanced micro– and mesoscopic fracture porosity; (3) fluid–rock interaction zones related to either alteration along structural discontinuities or to top–basement paleo–weathering profiles; (4) the buffering/sealing fault zones bounding the structural highs; (5) the sedimentary cover overlying the weathered crystalline basement acting as either reservoir rock, top–seal and/or source rock. The reservoir rock consists of the fractured and altered/weathered crystalline basement, in which fluid storage and transport are dependent mainly on the spatial arrangement, geometry and distribution of

3

63 "matrix" and "structural" permeability (Braathen et al., 2018; Trice et al., 2019). The "matrix"

64 permeability is directly related to the textural, compositional, and alteration characteristics of the host

65 crystalline basement (Bruhn et al., 1994; Géraud et al., 2010; Braathen et al., 2018). The "structural"

66 permeability, on the other hand, reflects and is related to the presence of structural discontinuities at

67 all scales, from microfractures to crustal–scale fracture and fault zones (Bruhn et al., 1994; Sibson

68 and Rowland, 2003; Holdsworth et al., 2020). Brittle faulting and fluid percolation within structural

69 discontinuities may either increase and/or decrease the matrix permeability of the host crystalline

70 basement (Bruhn et al., 1994; Caine et al., 1996; Holdsworth et al., 2019, 2020; McCaffrey et al.,

71 2020). The geological conditions (depth, pressure, temperature) and the origin (metamorphic,

72 hydrothermal, or meteoric) of fluids may lead to different brittle fault rock development and different

73 types of alteration from textural and compositional points of view (Steefel and Mäher, 2009).

74 The nature, spatial arrangement, and geometry of structural and textural features at the reservoir scale

75 are commonly defined through seismic geophysical investigations. Textural variations, fracture, and

76 fault zones displaying sufficient seismic impedance contrast as well as fault thickness or throws > 4–

77 10 m are usually detected by reservoir–scale seismic investigations and are thus classified as seismic–

78 resolution–scale (SRS) features (Tanner et al., 2019). However, the site– (well–, borehole– or tunnel–

79) scale fluid transport and storage capabilities are effectively controlled by sub–seismic–resolution

80 scale (SSRS) features (thickness/throw <4–10 m; Damsleth et al., 1998; Walsh et al., 1998).

81 In–situ analysis of outcrop analogues of onshore fractured and weathered basement blocks may

82 provide the unique opportunity to characterise the details of the petrophysical and mechanical

83 properties of SSRS features and to understand their relationships with larger, reservoir–scale SRS

84 features (Jones et al., 2008; Howell et al., 2014; McCaffrey et al., 2020; Primaleon et al., 2020). We

85 present here the results of the in–situ structural, geomechanical (uniaxial compressive strength, UCS),

86 and petrophysical (permeability, k) characterisation of selected outcrops of fractured and weathered

87 crystalline basement rocks on the island of Bømlo, western Norway (Fig. 1a–b). The crystalline

88   basement on Bømlo is being currently studied as the potential onshore analogue of fractured and

89   weathered basement reservoirs of the Utsira High, an economically viable unconventional reservoir

90   located offshore western Norway in the northern North Sea (Figs. 1a–2a; Banks et al., 2019; Trice et

91   al., 2019). The crystalline basement on Bømlo consists of igneous (granodiorite, granite and gabbro)

92   and volcano–sedimentary units of Ordovician–Silurian age belonging to the Upper Allochthon of the

93   Caledonian orogen (Slagstad et al., 2011). From the Permian onward, the crystalline basement on

94   Bømlo underwent a series of brittle deformation events (Scheiber and Viola, 2018) and experienced

95   pervasive alteration/weathering in response to subaerial exposure in tropical humid climate

96   conditions during the Triassic, forming a thick weathering profile (Fredin et al., 2017b). Similarly,

97   the offshore Utsira High reservoir is characterised by a pervasively fractured crystalline basement,

98   mainly composed of felsic intrusive and gabbroic rocks of Ordovician–Silurian age (Slagstad et al.,

99   2011; Riber et al., 2015), on top of which rests a paleo–weathering profile formed during the late

100   Triassic (Fredin et al., 2017b; Riber et al., 2017; Lothe et al., 2018) (Fig. 2b).

101   On Bømlo, we have worked on a few selected outcrops (Fig. 1c) that are representative of (1)

102   structural discontinuities affecting the crystalline basement "matrix" properties at different scales,

103   from SSRS fracture corridors to SRS fault zones (Fig. 2c) and (2) textural heterogeneities related to

104   the progressive development of alteration/weathering products(Fig. 2b). Our analyses aimed

105   specifically at the characterisation of the different structural and alteration products controlling the

106   current "matrix" mechanical and permeability properties of the crystalline basement at the sub–

107   seismic–resolution scale. The role of the different structural and alteration elements in controlling

108   fluid transport and storage, and the characterisation of potential reservoir rocks in fractured and

109   weathered crystalline basement structural highs, are then discussed to the benefit of broader, more

110   general conceptual scenarios.

111   Quantitative, high–resolution geomechanical and petrophysical datasets are quite rare, yet

112   fundamental for interpreting increasingly higher–resolution geophysical datasets, for reducing the

113 uncertainty in reservoir modelling, for better constraining fault zone mechanics and for assessing

114 borehole stability during exploration and drilling (Rutqvist and Stephansson, 2003; Wibberley et al.,

115 2008; Steer et al., 2011; Jeanne et al., 2017). Our results are thus useful to help bridge the gap between

116 field observations and large–scale geological contexts, where the lack of direct access to the

117 geological objects of interest and the processes determining their spatial and temporal evolution

118 commonly preclude straightforward across–scale correlations and quantifications. In addition, the

119 geological/structural contextualisation offered by the quantitative, high–resolution dataset presented

120 here may help to better read and interpret the at times overwhelming wealth of global and regional

121 geomechanical/petrophysical datasets (Lothe et al., 2018; Walter et al., 2018; Scibek, 2020).
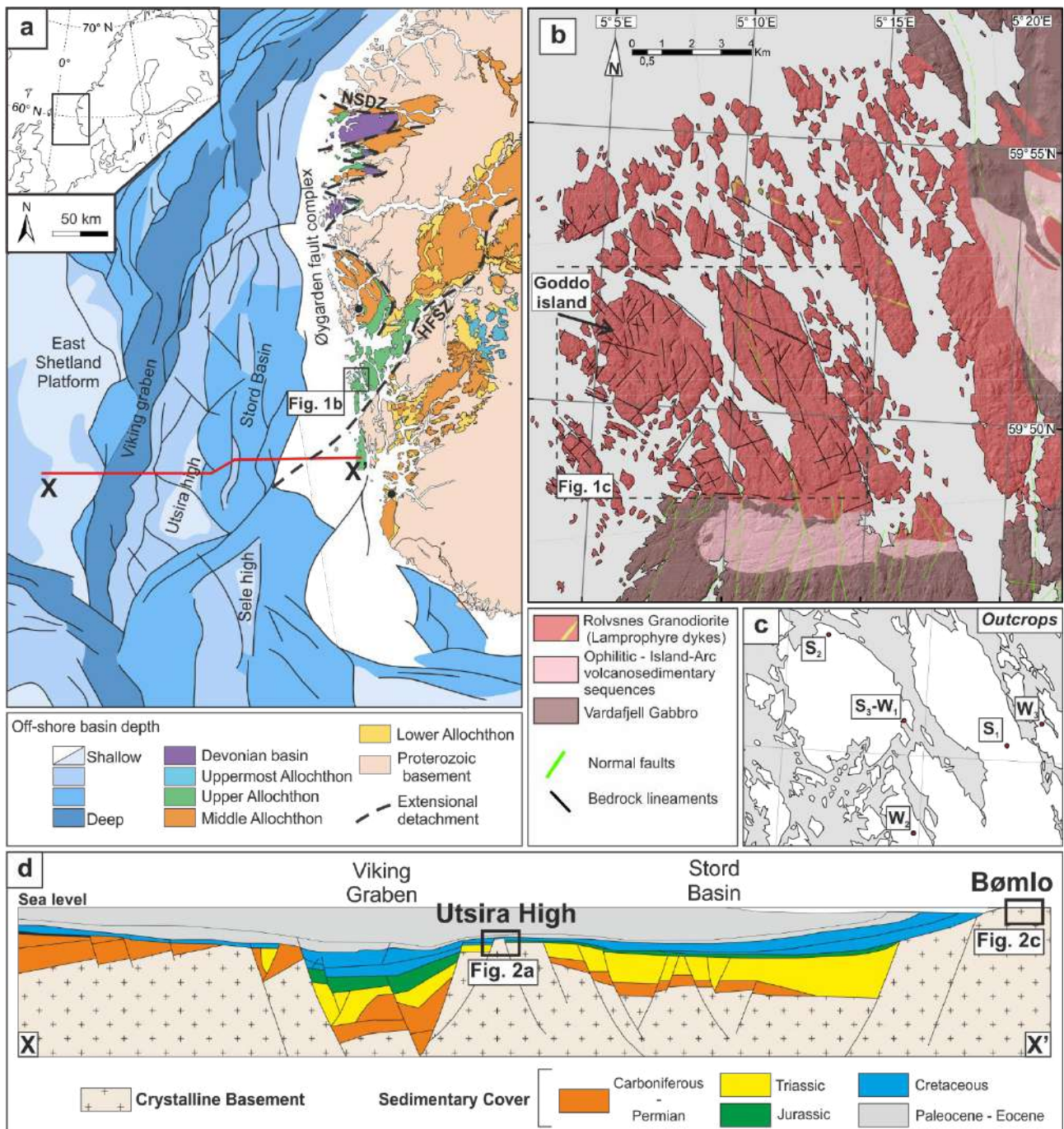
Figure 1: (a) Geological map of southwestern Norway and the northern North Sea (modified after Slagstad et al., 2011; Scheiber and Viola, 2018). HFSZ: Hardangerfjord Shear Zone; NSDZ: Nordfjord–Sogn Detachment Zone. The red line X–X' represents the trace of the geological cross section presented in Fig. 1d. (b) Geological map of the northern Bømlo area, including the island of Goddo (redrawn from the NGU geological map of Norway 1:50000). (c) Simplified topographic map of Bømlo showing the locations of the studied outcrops. (d) Schematic geological cross section through the central North Sea (X–X' in (a)) (modified from Riber et al., 2015).
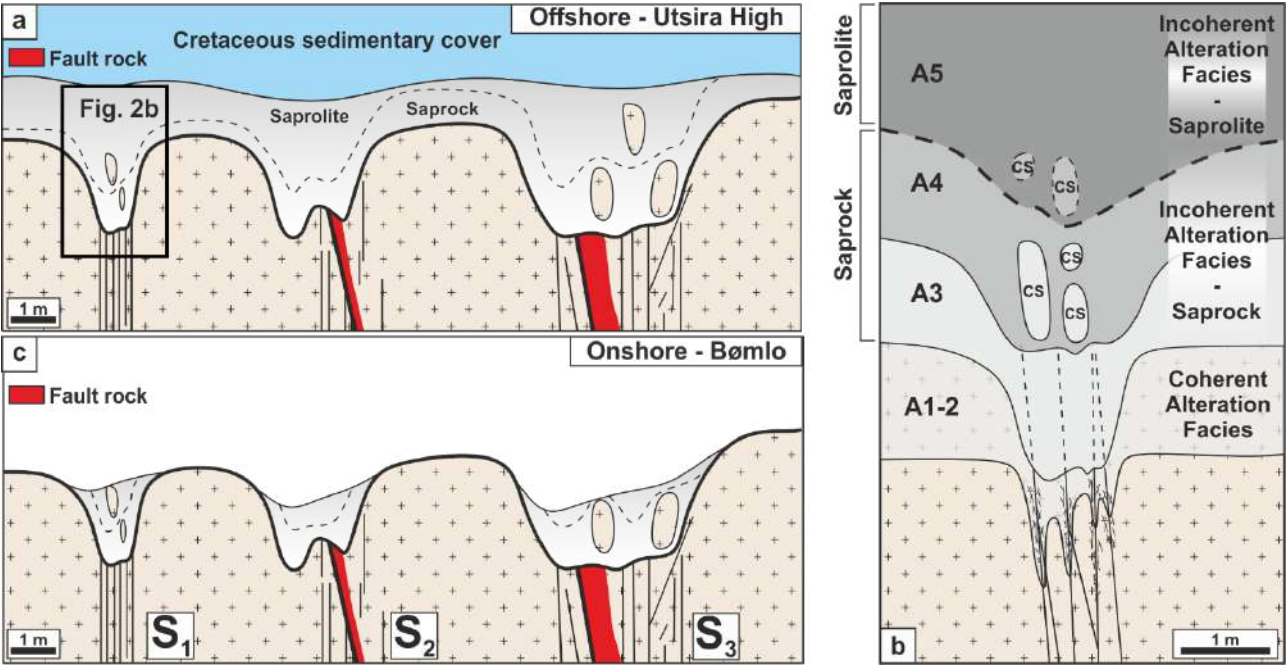
Figure 2: (a) Simplified schematic representation of the fractured and weathered basement top section preserved offshore in the Utsira High beneath the Mesozoic sedimentary cover. This schematic representation focuses on the fractured crystalline basement, which is characterised by different typologies of fractures and fault zones, the weathering profile (saprock–saprolite in grey) and the overlying sedimentary cover (light blue). The dashed line represents the boundary between saprock and saprolite within the weathering profile. (b) Simplified sketch of the top–basement weathering profile showing the gradual transition from unaltered and fractured host rock at the base of the profile, toward saprock and saprolite at the top. The weathering profile locally reaches greater depths where in correspondence with structural discontinuities (in this case, a SSRS fracture corridor, S_1 of Fig. 2a and 2c). The progression of weathering is illustrated by the continuous darkening of the grey shades and the increasing number in the alteration/weathering grade on the left (A1–A5). (CS: core stones). (c) Simplified schematic representation of the fractured and weathered basement top section now exposed onshore on the island of Goddo. The erosion of the weathering profile has led to the exposure of an "etched" basement top surface (Fredin et al., 2017). S_1, S_2 and S_3 represent the three typologies

146   of deformation structures studied in this work. S_1: SSRS fracture corridors; S_2: SSRS fault zone; S_3:

147   SRS fault zone.

148

149

2. Geological setting

The crystalline basement rocks exposed on the island of Bømlo in western Norway belong to the Upper Allochthon units of the Caledonian orogen (Gee et al., 2008) (Fig. 1a). They mainly consist of variably metamorphosed igneous, volcanic and sedimentary units derived from the Iapetus oceanic domain (Roberts, 2003). The study area is located within the Rolvsnes granodiorite (RGD, 466 ± 3 Ma, U/Pb on zircon) (Scheiber et al., 2016), a plutonic body related to pre–Scandian magmatism that intrudes the ophiolitic, gabbroic, and volcano–sedimentary orogenic units (Slagstad et al., 2011) (Fig. 1b). After its emplacement in the Ordovician, the RGD remained at shallow crustal levels (< 10–15 km depth), thus escaping pervasive ductile deformation and metamorphic re–equilibration during the Scandian tectonometamorphic event (Scheiber et al., 2016; Scheiber and Viola, 2018). During the post–Caledonian orogenic collapse and extension, the Upper Allochthon units in the Bømlo region belonged to the hanging wall of the Hardangerfjord Shear Zone, a regional NW–dipping extensional detachment reactivating earlier Caledonian thrusts and nappe contacts (Fig. 1a) (Fossen and Hurich, 2005). The RGD recorded a prolonged and multi–phased brittle deformation history, which has been characterised in detail by means of structural and geochronological analysis of the different fracture patterns exposed on Bømlo (Scheiber et al., 2016; Scheiber and Viola, 2018).

2.1 Brittle deformation and alteration history of the Bømlo basement

The latest stages of Caledonian compression during the Mid Ordovician–Silurian are recorded by ENE–WSW–striking reverse and kinematically consistent conjugate sets of strike–slip shear fractures and minor faults accompanied by the emplacement of greisens, dykes, and mineralised veins (Scheiber et al., 2016). A first phase of NW–SE extension occurred during the Devonian in response to Caledonian orogenic collapse, as recorded by the development of minor, NE–SW–striking normal faults. Ordovician to Devonian mineralised veins, joints, shear fractures, and minor faults are pervasive and widely distributed, and they are commonly filled with– and sealed by a variety of minerals. In the Permian–Early Cretaceous, the area underwent renewed regional extension related

to the long–lived series of E–W–directed North Sea rifting events. The first main North Sea rifting stage is recorded by the development of widespread NE–dipping normal faults active during Permian to Triassic times (Viola et al., 2016; Scheiber and Viola, 2018). This rifting event led to the formation of the most prominent structural highs and basins of the North Sea, namely the Stord Basin, Utsira High, and the Viking Graben (Bell et al., 2014; Scheiber and Viola, 2018). Rifting and crustal stretching continued during the Late Triassic and Jurassic leading to the formation of ENE–dipping normal faults associated with the deepening and development of the offshore Viking Graben (Scheiber and Viola, 2018) and the progressive reactivation of the previously formed NE–dipping normal faults (Viola et al., 2016). This rifting phase enhanced the rapid exhumation of the Bømlo crystalline basement from 6–8 km to shallow (<2 km) depths during Permian–to–Jurassic times (Scheiber and Viola, 2018). From the Late Jurassic onward, the crystalline basement has resided at very shallow depth (<2 km; Fredin et al., 2017b; Scheiber and Viola, 2018). Far–field stresses related to the Early Cretaceous rifting stage of the northern North Sea and the Mid–Norwegian margin subsequently led to the development of N–S–trending fracture corridors in the Bømlo region (Viola et al., 2016; Scheiber and Viola, 2018).

A distinctive characteristic of the Bømlo fractured crystalline basement is the occurrence of alteration and weathering products spatially related to fracture and fault zones (Viola et al., 2016; Fredin et al., 2017b; Scheiber and Viola, 2018). Altered/weathered granodiorite is invariably found as lenses along fractures and variably altered volumes within high–fracture density deformation zones. The dense network of fractures and fault zones likely promoted fluid infiltration at depth (Place et al., 2016). K–Ar dating of alteration–related authigenic illite has revealed the occurrence of multiple shallow–crustal levels alteration/weathering events during the prolonged and multi–phased brittle deformation history discussed above (Viola et al., 2016; Fredin et al., 2017b; Scheiber and Viola, 2018). A significant event occurred during the Late Triassic (ca. 220–200 Ma), when the fractured crystalline basement on Bømlo was exposed to sub–aerial alteration and formation of deep–weathering horizons

11

(saprock – saprolite) related to the Mesozoic tropical–humid climate of the region (Fredin et al., 2017b). Other alteration events likely occurred in the Permian and Jurassic–Cretaceous (A. Margreth personal communication; Viola et al., 2016; Scheiber and Viola, 2018). The detailed genetic processes and geological conditions under which these latter alteration events occurred are still not well constrained (A. Margreth personal communication). Despite the possible diachronism and superposition of different alteration/weathering events, all the observed alteration products of the crystalline basement on Bømlo present similar field textural and mineralogical characteristics. Progressive disaggregation of the host RGD into sandy "grus–type" aggregates (*sensu* Migoń and Thomas, 2002) is commonly accompanied by mineral (feldspar) alteration and clay–mineral authigenesis. Such characteristics are ascribable to a process of arenitisation, kaolinitisation, and/or saprolitisation of the host RGD occurring at shallow crustal depths (< 6 km) up to surficial conditions (Viola et al., 2016; Fredin et al., 2017b, 2017a; Scheiber and Viola, 2018). It is indeed quite well known that hydrothermal kaolinitisation and saprolite formation under tropical–humid climate conditions may lead to alteration products with similar textural/mineralogical/mechanical characteristics (Coggan et al., 2013).

2.2 Onshore–offshore correlation – Bømlo basement and Utsira High

Alteration characteristics similar to those documented onshore have been detected in offshore exploratory wells from the Utsira High fractured crystalline basement at variable depth beneath the sedimentary cover (Riber et al., 2015; Trice et al., 2019). Amidst the central North Sea, the Utsira High represents a N–S trending basement structural high bounded by the Viking Graben to the west and the Stord Basin to the east (Fig. 1a, d) (Gabrielsen et al., 2001). The basement unit in its core is mainly composed of Ordovician–Silurian granitoid and gabbroid rocks (Riber et al., 2015). Petrological, geochronological, and geophysical data suggest that, prior to the opening of the North Sea, the crystalline basement of Bømlo and the basement units of the Utsira High likely belonged to the same unit of the Upper Allochthon (Slagstad et al., 2011; Lundmark et al., 2014; Riber et al.,

225 2015; Fredin et al., 2017b; Lothe et al., 2018; Trice et al., 2019). The seismically imaged top–

226 basement topography of the Utsira High shows the occurrence of widespread fracture lineaments and

227 fault zones , resembling the onshore joint–aligned valley morphology of the Bømlo region (Fredin et

228 al., 2017b). The pervasive and variably oriented fracture lineaments and fault zones thus suggest that,

229 similarly to the onshore margin, the Utsira High also underwent a prolonged and multi–phased brittle

230 deformation history (Fredin et al., 2017b). Brittle deformation probably started in the Permian–

231 Triassic during the first rifting phase of the North Sea, and ended in the Cretaceous–Paleogene with

232 the northward migration of the rifting activity toward the Mid–Norwegian margin (Bell et al., 2014;

233 Scheiber and Viola, 2018). Offshore exploration wells have identified the occurrence of a variably

234 preserved 1–10 m thick weathering profile atop of the fractured granitoid basement (Fig. 2a) (Riber

235 et al., 2015; Trice et al., 2019). The weathering profile, from top to bottom, consists of (Fig. 2b)

236 (Riber et al., 2015, 2016, 2017, 2019a): (i) clay–rich, saprolite – incoherent alteration facies A5 of

237 Riber et al., (2016); (ii) grus–type saprock, in which the granitoid magmatic texture is still preserved

238 – incoherent alteration facies A3–A4 of Riber et al., (2016); (iii) coherent, partially weathered

239 granitoid, still preserving the magmatic texture and mechanical properties of the host rock – alteration

240 facies A1–A2 of Riber et al., (2016). K–Ar dating on authigenic illite from core samples of the

241 saprolitic level in the weathering profile has shown that the Utsira High crystalline basement was

242 exposed to sub–aerial conditions and weathering during the Triassic (206 ± 4 Ma) (Fredin et al.,

243 2017b).

244 After the Late Triassic, burial and sedimentation affected the whole passive margin (including the

245 Utsira High and Bømlo region), causing the deposition of a several km thick Mesozoic sedimentary

246 succession (Sclater and Christie, 1980; Gabrielsen et al., 2001; Bell et al., 2014). The buried Utsira

247 High fractured–and–weathered basement acted as a system reservoir–trap for oil and currently, thus,

248 represents an economically viable unconventional oil play (Trice et al., 2019). Offshore exploration

249 wells have identified exploitable oil resources hosted in the basement–top weathering profile beneath

the sedimentary cover (Fig. 2a–b) (Riber et al., 2015, 2017). Pre–Cretaceous SRS faults bound laterally the reservoir basement blocks, which are overlain by the Jurassic–Cretaceous sedimentary cover that acted as both lateral source rock and top–seal unit for oil–migration within the structural high (Trice et al., 2019). Jurassic–Cretaceous sedimentation likely affected also the Bømlo region, as inferred from the occurrence of Late–Mesozoic sedimentary basins close to the present–day onshore area (Fredin et al., 2017b, 2017a). Onshore, the Mesozoic sedimentary cover and the underlying Triassic top–basement weathering profile have been almost completely eroded by geomorphic and glaciogenic processes during the Cenozoic (Fredin et al., 2017b; Riber et al., 2017). As a consequence, only the deepest portions of the top–basement weathering profile are locally preserved, particularly where the effects of weathering penetrated for a few tens of m into the crystalline basement along discrete structural discontinuities (i.e. fracture and fault zones; Fig. 2c) (Fredin et al., 2017b). The deepest portion of the weathering profile, preserved in these structurally–controlled depressions may, therefore, have escaped from significant textural, mechanical, and mineralogical modifications related to the subsequent Cenozoic erosion, weathering or alteration (Fredin et al., 2017b, 2017a; Lothe et al., 2018)

For these reasons, an increasing number of multidisciplinary studies in the region considers the fractured and weathered crystalline basement exposed on Bømlo as a reliable onshore analogue of the offshore crystalline basement of the Utsira High (Fredin et al., 2017b; Lothe et al., 2018; Banks et al., 2019; Trice et al., 2019).

3. Methods

Our structural analysis focussed on the identification and characterisation of meso–scale fracture patterns and the definition of the main structural domains related to faulting. The investigation of petrophysical (permeability) and geomechanical (uniaxial compressive strength) properties has been carried out directly in the field on selected representative outcrops. In–situ permeability

14

275 measurements have been carried out with a New England Research TinyPerm–3 air–

276 minipermeameter on both fault rocks and alteration products related to basement weathering and

277 saprolitisation. The minipermeameter is calibrated by the manufacturer with known standards. The

278 instrument allows a reliable field investigation of rock permeability within small volumes (1–1.5 cm^3)

279 in the 10^{-3}–10 D range, even though controlled laboratory tests have demonstrated its capability to

280 measure permeability values as low as 10^{-5} D (Filomena et al., 2014). In the bulk–rock permeability

281 mode, the instrument directly yields an estimate of the permeability based on the outgoing air flow

282 rate from the built–in compression vessel. Permeability values obtained from air–minipermeametry

283 need to be corrected and standardised in order to be comparable with permeability values obtained

284 from laboratory tests on rock plugs or image analysis (Fossen et al., 2011; Filomena et al., 2014;

285 Torabi et al., 2018). Air–minipermeameters yield either larger permeability values (by a factor of

286 1.7–1.8) when compared with results derived from image analysis quantifications (Fossen et al.,

287 2011), or lower permeabilities (-37%) than those obtained from small (<10 cm) rock plugs used in

288 laboratory tests (Filomena et al., 2014). In addition, permeability estimates from permeametry tests

289 adopting a gas as permeating fluid (as in air–minipermeametry) can be significantly larger than the

290 estimates from permeability tests relying on a liquid as permeating fluid as a consequence of possible

291 slip–flow effects (Klinkenberg effect) (van Noort and Yarushina, 2019). This has to be considered

292 when using absolute gas permeability values to analyse the flow of a liquid in the same porous

293 medium.

294 The geomechanical characterisation has been carried out with a L–type Schmidt hammer (DRC

295 GeoHammer, 0.735 N·m impact energy) calibrated according to international standards (ASTM

296 D5873–00; EN 12 504–2; ASTM C 805–02). The reliability range of the instrument extends between

297 10 MPa and 300 MPa of UCS (Aydin and Basu, 2005).

298 We ran petrophysical and geomechanical analyses both on compositionally and texturally

299 homogeneous volumes of the outcrops, thought to be representative of the bulk rock properties, and

along transects. Where rock textural anisotropies were present, we performed permeability and
Schmidt hammer analysis both perpendicular and parallel to the dominant planar rock fabric, aiming
at evaluating the potential anisotropy of petrophysical and geomechanical properties. Transects
allowed us to constrain the variation of the analysed properties across weathering fronts and high–
density fracture zones. Surface spot analyses for both permeability and Schmidt hammer rebound
analyses have been done by probing representative outcrop surfaces with at least 10 measurements.
Selected measuring spots were at least 10–15 cm away from mesoscopic fractures wherever possible
(Aydin and Basu, 2005). Both permeability and Schmidt hammer rebound analyses were repeated
twice in the immediate surroundings of the selected spot along transects, for a total of three
measurements. The replicates were not exactly on the same point to avoid results biased by subtle
rock modifications (e.g., compaction and microfracturing) due to the previous measurements. Each
measure spot was kept at c. 5–10 cm from the nearest measuring point both along transects and within
selected areas, and taken to be representative of a 5 cm–radius hemispherical volume below it (ASRM
standards; Aydin and Basu, 2005; Aydin, 2009; Demirdag et al., 2009). UCS values were retrieved
from the analysis of Schmidt hammer rebound values (Aydin and Basu, 2005). Schmidt hammer
measurements were carried out perpendicularly to clear, fresh rock surfaces (wherever possible),
parallel to the horizontal direction. Schmidt hammer rebound values obtained from the in–situ
measurement were converted into UCS by following the hammer orientation–dependent calibration
curves provided by the manufacturer. Horizontal rebound values were converted into UCS by the
following equation:

$$UCS = 0.0232 * R^{2.2637} \text{ (MPa)}$$

Presented data are not corrected or standardised, so as to fully capture the heterogeneity and potential
spread of rock mechanical properties (Aydin, 2009).

At one outcrop, fracture pattern characteristics have been quantified by using circular scan windows
along a transect previously adopted for petrophysical and geomechanical analysis (Watkins et al.,

325   2015). The results of fracture intensity (P_{21}) quantification from circular scan windows 10–cm–

326   diameter have been compared with the along–transect variation of mechanical strength (Vignaroli et

327   al., 2019). The same outcrop has been analysed also with a 1.4 m radius circular scan window to

328   capture the outcrop scale characteristics of the fracture pattern. A schematic representation of the

329   tectonic fractures of the outcrop has been obtained by line drawing on an outcrop field photo. The

330   resulting line drawing has been analysed with FracPaQ (Healy et al., 2017) in order to quantify

331   fracture intensity and 2D permeability at the outcrop scale in the direction of fluid flow (Long et al.,

332   1982; Watkins et al., 2018).

333

334   **4. Results**

335   *4.1 Outcrop description*

336   On Bømlo, we have investigated five outcrops representative of the different deformation and

337   weathering product end members, to constrain their mesoscopic structural characteristics as well as

338   their petrophysical and geomechanical properties. Some of the analysed outcrops contain both

339   structural and weathering features. For the clarity of presentation and discussion, outcrops are

340   grouped into Group S (representative of *structural features*, S_1 to S_3) and Group W (*weathering*

341   *features*, W_1 to W_3) (Figs. 1c, 2c–d). Magmatic dykes, greisens and mineralised veins are common

342   in the RGD. The detailed characterisation of their mechanical strength and permeability properties is,

343   however, beyond the scope of this paper.

344   Group S includes outcrops where we measured the geomechanical and petrophysical characteristics

345   of discrete mesoscopic deformation zones (Fig. 2c). Our field investigations focussed mainly on the

346   analysis of fracture corridors and major (either SSRS or SRS) fault zones formed during the Permian

347   to Cretaceous interval, which significantly contributed to the development and modification of the

348   crystalline basement permeability (Scheiber and Viola, 2018; McCaffrey et al., 2020). The pervasive

349   and widely distributed Ordovician to Devonian mineralised joints, shear fractures and minor faults

are commonly filled and sealed by different minerals (Scheiber and Viola, 2018), such that their

contribution to the overall current permeability of the crystalline basement is assumed to be very

limited (Watkins et al., 2018; McCaffrey et al., 2020). The field criteria adopted for the classification

of different structures include: (i) the width of the deformation zone, as indicated by the across–strike

thickness of the fractured domain; (ii) the occurrence/lack of fault rocks within the deformation zone;

(iii) the width of the fault rock–bearing deformation zone (fault core). The width of the fault core may

help us to quantify the minimum fault throw, and thus discriminate between SSRS and SRS

deformation zones. The structural features included in Group S are: SSRS fracture corridors (S_1), a

SSRS fault zone (S_2), and a SRS fault zone (S_3). Group S is numbered according to the increasing

size of the studied structural features (fracture/fault zone width) as constrained by outcrop

observations. The analysis of these outcrops allowed us to constrain the mechanical strength and

permeability variation related to: (1) high–intensity fracture zones within (SSRS) fracture corridors;

(2) fault rock development and distribution within SSRS and SRS fault cores.

Group W includes outcrops used to characterise the weathering features affecting the crystalline

basement. Each Group W outcrop has already been previously analysed and sampled for illite K–Ar

dating aiming at constraining the age of weathering (Viola et al., 2016; Fredin et al., 2017b; Scheiber

and Viola, 2018). Results from XRD analysis (Table 1) reported in the cited references are here

adopted to qualitatively characterise the mineral composition of weathering products. Group W

includes: outcrop W_1 formed by partially altered RGD with incipient weathering and discolouring

mainly localised along fractures; outcrop W_2 formed by cohesionless, altered RGD, still preserving

the RGD magmatic structure but completely transformed into a sandy aggregate (saprock – grus);

outcrop W_3 formed by cohesionless, altered RGD with increasing clay content (saprolite). The W

outcrops are presented herein from W_1 to W_3 according to the increasing degree of weathering (from

incipient to evolved weathering). The degree of weathering has been qualitatively deduced directly

on the field comparing the mechanical/textural characteristics of the weathering products with those

18

375 described by Riber et al. (2016) for the alteration facies of the Utsira High core samples. In all the

376 analysed outcrops, alteration/weathering products invariably postdate the formation of brittle

377 deformation zones.

378

379   *4.1.1 Group S – Fractures and fault zones within the crystalline basement*

380 **Outcrop S$_1$.** This outcrop contains a deformation zone defined by a 10–15 m thick fracture corridor.

381 The central portion of the fracture corridor is characterised by a 2–5 m thick zone of high fracture–

382 intensity (average fracture spacing = 0.05–0.1 m), composed of NNE–SSW–trending subvertical

383 open fractures (Fig. 3a). Mesoscopic fractures are usually longer than 0.5–1 m along the dip direction,

384 generally subparallel, but still locally forming a well–interconnected fracture network. Their typical

385 aperture (*sensu* Ortega et al., 2006) is in the order of <1 mm. This deformation zone likely

386 accommodated minor (<1m) lateral displacement, as inferred by the only local and rare development

387 of fault striae (mainly strike–slip) on fracture surfaces and the limited offset (c. 6 cm) of crosscut

388 magmatic markers (Scheiber and Viola, 2018). The outcrop is generally fresh, although fractures are

389 in some cases filled with granular material probably related to either alteration or presence of fault

390 rocks along the major fracture planes. The presence of now–eroded saprolite horizons has been

391 inferred above the outcrop (Fig. 6g–h in Scheiber and Viola, 2018). The finest grain–size fractions of

392 the alteration rock observed within the fractures are enriched in smectite–like clays of Jurassic age

393 (187.5 ± 16.7 Ma; Table 1), as inferred from K–Ar dating on authigenic illite (sample TSC–1 of

394 Scheiber and Viola, 2018). Alteration of the rock postdates the formation of the fracture corridor,

395 which is thus older than Jurassic in age. The only limited throw (< 1 m) and width of the fracture

396 corridor core (< 10 m) suggest that outcrop S$_1$ represents a SSRS fracture corridor.

397

19

Outcrop S$_2$. Outcrop S$_2$ contains two subparallel, well–localised SSRS fault zones characterised by a 10 cm thick cataclastic fault core (Fig. 6i–j in Scheiber and Viola, 2018). Each fault zone is characterised by a polished principal slip surface (PSS) oriented 70°/140° (dip/dip direction) (Fig. 3b). The PSS is decorated by transtensive–kinematics slickenlines plunging 30°/070° (plunge/trend). Several scattered, sub–vertical open fractures surround the fault core, defining a poorly developed 1–m–thick damage zone. Speculatively, the thickness of the fault core (10 cm) would be consistent with a fault throw in the order of 1–10 m (Torabi and Berg, 2011). The limited fault core width and estimated throw suggest that these fault zones may represent SSRS fault zones. The host RGD and the cataclastic core are locally altered, as documented by the occurrence of an irregular volume of sandy material (Fig. 3b). The alteration product is characterised by an increasing kaolinite content over smectite (sample TSC–36 of Scheiber and Viola, 2018). K–Ar dating on authigenic clays constrains alteration to the Cretaceous (127.4 ± 16.5 Ma, Table 1). Therefore, the age of faulting must be older than Cretaceous in age.

Outcrop S$_3$. The Goddo Fault Zone (GFZ) crops out along a road cut on the island of Goddo (northwestern Bømlo, Figs. 1b–4). The GFZ represents a E–dipping normal fault zone formed and reactivated during Permian–to–Cretaceous extensional tectonics (Viola et al., 2016; Fredin et al., 2017b; Scheiber and Viola, 2018). It is characterised by two separate and distinct fault cores (marked as S$_{3A}$ and S$_{3B}$ in Fig. 4a–b), separated and surrounded by highly fractured damage zones (Figs. 4a–b, 5a–b). The two fault cores consist of several brittle structural facies (*sensu* Tartaglia et al., 2020), i.e. different fault rocks characterised by different texture, mineralogical assemblages, and ages of formation (Viola et al., 2016). Brittle structural facies observed within the fault core include: (a) a polished PSS overlain by (b) a massive, well–sorted clay–rich gouge, (c) a phyllonitic gouge, and (d) a cohesive cataclasite (Fig. 5a–d). The PSS of the GFZ consists of a 1–2 cm-thick fine–grained quartz–coated polished surface, dipping 50°/070° and bearing dip–slip slickenlines (50°/070°)

423 associated with top–to–the–east normal fault steps (Fig. 5c–d). The overlying gouge core is 20–30

424 cm thick and it is composed of two main gouge layers showing different textures and age of formation

425 (Viola et al., 2016). The clay–rich gouge consists of a 5–10 cm thick homogeneous and isotropic

426 plastic gouge (Fig. 5c–d). The phyllonitic–gouge consists of a scaly, phyllosilicate–rich gouge

427 containing a pervasive S–C' composite fabric (Fig. 5d). K–Ar illite dating showed that the phyllonitic

428 gouge of the fault core S_{3B} developed during Permian extension (264.1 ± 5.4 Ma; Table 1); Triassic–

429 Early Jurassic fault reactivation led to the formation of the clay–rich gouge and reworking of the

430 phyllonitic gouge in the S_{3B} fault core (200.2 ± 4.1 Ma; Table 1) (Viola et al., 2016). The gouges are

431 overlain by a 20–40 cm thick layer of indurated cataclasite, containing internal discrete shear planes

432 decorated by purple–reddish–orange coatings of Fe–oxides (Fig. 5d). The occurrence of fault rocks

433 is limited to the two described fault cores. The phyllonitic gouge is only observed in the S_{3B} fault core

434 (Fig. 5d). No fault breccia bounding the fault core is observed.

435 The thickness of each fault core is in the order of 0.6–1 m (Fig. 5c–d), suggesting that each fault core

436 may have accommodated a cumulative normal throw of 10–100 m (Torabi and Berg, 2011), thus

437 defining a valuable example of a SRS fault zone (Viola et al., 2016). Accordingly, the damage zone

438 width would be in the order of 10 to 100 m (Wilson et al., 2003; Faulkner et al., 2006, 2010). The

439 damage zone is characterised by densely spaced (average spacing = 0.1–0.5 m) mesoscopic fractures

440 related to both the background basement fracturing and to the GFZ itself (Scheiber and Viola, 2018).

441 The GFZ damage zone is well exposed in the footwall, and between fault cores, whereas the geometry

442 and exposure of the outcrop did not allow us to quantify the exact thickness of the hanging wall

443 damage zone and the entire fault zone in the field (Fig. 4).

444 *4.1.2 Group W – Weathered outcrops*

445 **Outcrop W₁.** The outcrop is in the same locality of outcrop S_3–GFZ. The whole GFZ is crosscut by

446 a series of poorly exposed alteration/weathering zones (outcrops marked with W_{1A}–W_{1B} in Fig. 4a;

447 Fig. 6a–b). These weathering zones are spatially related to NNE–SSW, 1–2 m thick fracture corridors

448 cutting across both the undeformed RGD host (Fig. 6a) and fault rocks (Fig. 6b) (Viola et al., 2016;

449 Scheiber and Viola, 2018). The granodiorite within the fracture corridor mostly preserves its primary

450 structure and cohesion at the hand specimen scale. Partially altered host rock lithons within the

451 fracture corridor are embedded in a cohesionless granular matrix, mainly composed of quartz and

452 clay minerals, which forms much less than 50 vol% of the altered outcrop (Fig. 6a–b). The

453 mineralogical composition of the finest fraction of this matrix is dominated by smectite, as inferred

454 from the sample BO–OFR–1 presented in Viola et al. (2016) and Fredin et al. (2017b). The

455 weathering material included therein has been dated to the Early Cretaceous (125.2 ± 4.2 Ma, Table

456 1). The mineralogical composition and textural characteristics of the weathering products suggest that

457 this outcrop is equivalent to the alteration facies A1 described by Riber et al. (2016).

458 **Outcrop W$_2$.** Outcrop W$_2$ is characterised by the occurrence of a pervasive NNW–SSE–trending

459 fracture set (Fig. 6c). Fractures are preferentially organised in 1-m-thick clusters, separated by 2–5 m

460 of non–fractured RGD host. Commonly, rock volumes within fracture clusters are heavily altered and

461 transformed in a variably cohesive granular material preserving the magmatic fabric. Measurements

462 were performed along a transect perpendicular to the main fracture trend, on a vertical surface and

463 crossing through an alteration zone exhibiting a variable degree of weathering (from left to right in

464 Fig. 6c). Qualitatively, the outcrop was subdivided into three main domains: (i) partially altered host

465 granodiorite with some localised mesoscopic fractures (domain *d1* in Fig. 6c), (ii) granular

466 cohesionless aggregate preserving the granodiorite fabric but no mesoscopic fractures (domain *d2* in

467 Fig. 6c), (iii) granular aggregate with increasing clay content (domain *d3* in Fig. 6c), as inferred from

468 plastic deformation of hand samples. Unpublished K–Ar illite dating data suggest that this alteration

469 is older than Triassic and its mineralogical composition dominated by smectite (A. Margreth personal

470 communication). As reported earlier, similar weathering characteristics have been observed in

471 outcrop S$_2$.

22

472   **Outcrop W$_3$.** The outcrop is characterised by a 2 m thick altered rock volume within granodiorite,

473   bounded by N–S trending fractures. The altered volume consists of a cohesionless granular aggregate,

474   grading from saprock to mature, fine–grained clay–rich saprolite, enveloping variably altered "core

475   stones" (i.e., remnant blocks of granodiorite less weathered than the embedding material and resulting

476   from spheroidal weathering processes; cfr.Ryan et al., 2005; Fig. 6d) (Fredin et al., 2017b, 2017a).

477   Weathering products in outcrop W$_3$ are well represented by the samples (Bomlo2–3–4) analysed by

478   Fredin et al. (2017a,b), with a predominantly kaolinitic composition and likely developed during sub–

479   aerial exposure of the crystalline basement in the Triassic (220–200 Ma, Table 1; Fredin et al., 2017b).

480

481

| Outcrop | Sample ID | Grain Size (µm) | XRD Data | | | | | | | | | K-Ar Dating | | Ref. |
			Quartz	Kaolin	Illite/Mica 2M1	Illite/Mica 1M	Dioctahedral smectite	Interstratified illite/smectite	Albite/Anorthite	Anatase	Lepidocrocite	Age (Ma)	Error (Ma)	
S1	*TSC-1*	0.1 - 0.4		5			95		<1			**187.5**	**16.7**	[3]
		0.4 - 2	<1	9			87		4			192.6	13.7	
		2 - 6	1	18			75		6			260.4	8.1	
S2	*TSC-36*	<0.1		7			93					**127.4**	**16.5**	[3]
		0.1 - 0.4		25			75		<1	<1		177.6	16.2	
		0.4 - 2	<1	29	2		67		2	<1		261.7	8.4	
		2 - 6	<1	22	4		71		3	<1		324.0	9.0	
S3	*BO-GVI-1*	<0.1		1	20			79				**200.2**	**4.1**	[1]
		0.1 - 0.4		5	21		6	68				218.9	4.4	
		0.4 - 2	3	16	28		24	29		<1		240.7	5.0	
		2 - 6	34	8	14		13	30	1			272.1	5.5	
		6 - 10	35	8	17		12	27	1			282.9	5.7	
	BO-GVI-2	<0.1	<1	12	14	4	20	49	1			**264.1**	**5.4**	[1]
		0.1 - 0.4										262.0	5.3	
		0.4 - 2										303.8	6.3	
		2 - 6	2	9	32	2	16	35	4			349.6	7.1	
		6 - 10	2	9	33	4	17	31	4			354.4	7.1	
W1	*BO-OFR-1*	<0.1		7			93		<1			**125.2**	**4.2**	[1]
		0.1 - 0.4		7			93		<1			121.4	5.3	
		0.4 - 2		16			82		2			167.7	6.5	
		2 - 6	<1	22	3		71		3	<1		272.1	5.8	
		6 - 10	<1	25	2		68		4	1		287.5	6.2	
W3	*Bømlo 2*	<0.1					89				11	**210.0**	**13.1**	[2]
		0.1 - 0.4		4			78		2		16	290.2	10.6	
		0.4 - 2	<1	7			83		3		7	307.5	38.3	
		2 - 6	<1	8	6		79		3	<1	4	406.9	20.3	
	Bømlo 3	<2	<1	76	1		23					**217.3**	**4.8**	[2]
		2 - 6	<1	72	3		24							
	Bømlo 4	<2	<1	53			46		1			**233.0**	**5.0**	[2]
		2 - 6	<1	53	2		43		2					

Table 1. XRD data and K–Ar dates from synkinematic/authigenic illite samples of the outcrops studied in this paper. References: [1] Viola et al. (2016); [2] Fredin et al. (2017b); [3] Scheiber and Viola (2018).
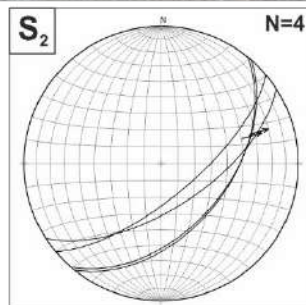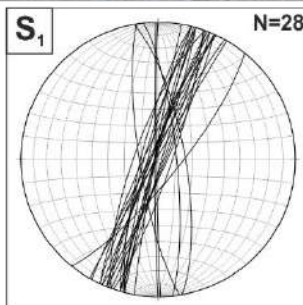
489   **Figure 3**: (a) Fracture corridor at outcrop S_1. (b) The fault zone of outcrop S_2 is characterised by a

490   thin, well–localised, gouge– and cataclasite–rich fault core enveloped by a 1 m thick, poorly–

491   developed damage zone. Fluids percolating through the fault core led to the alteration of cataclasite

492   and the damage zone observed in the central portion of the image. PSS: Principal Slip Surface.

493   Stereonets: Lower hemisphere, equal area projection of fractures and fault planes. The black arrows

494   represent the direction of movement of the hanging wall along the fault plane.
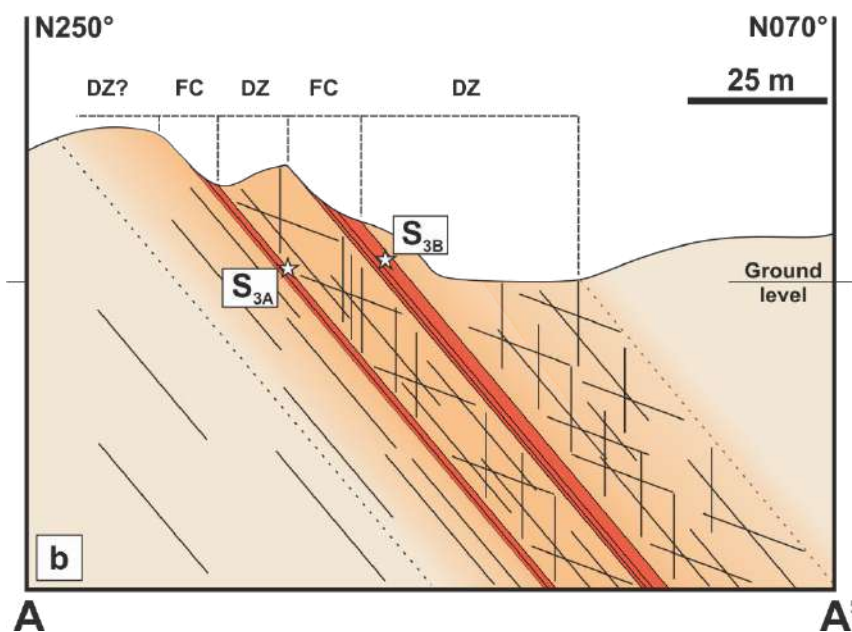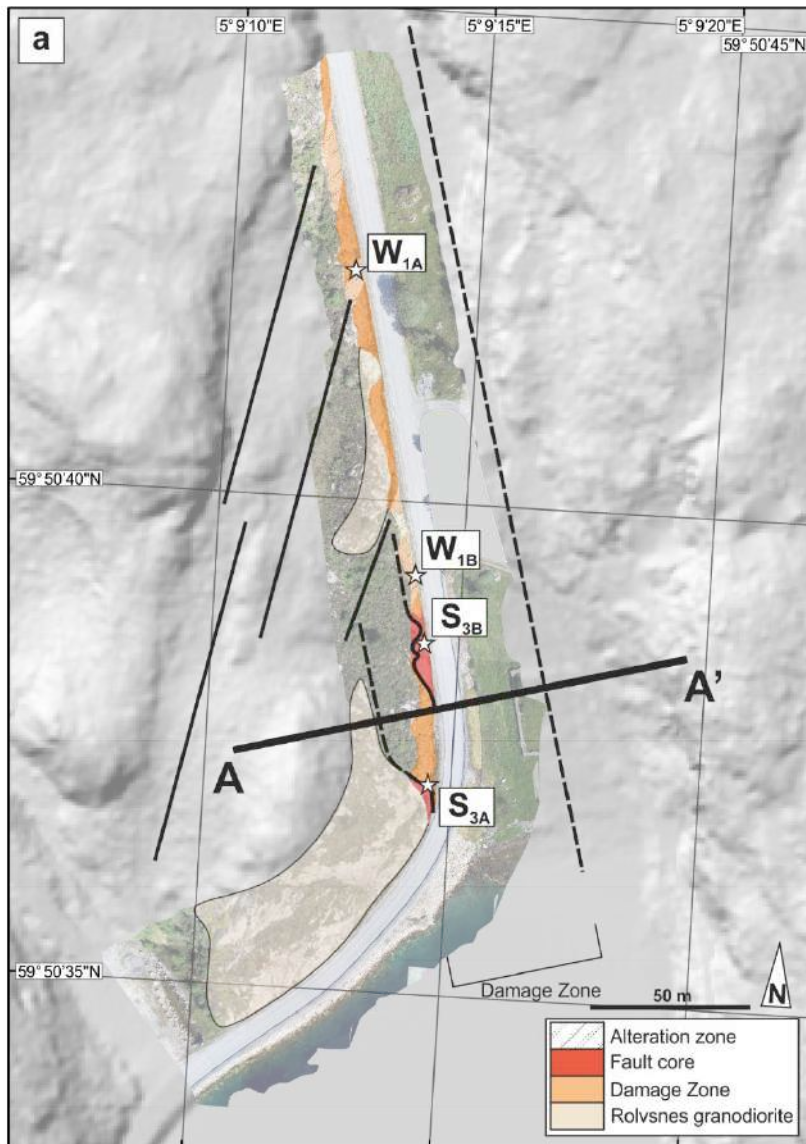
496   **Figure 4**: (a) Schematic map of the Goddo Fault Zone (outcrop S$_3$) overlain on a composite UAV

497   orthophoto and LiDAR digital elevation model image. The location of the studied outcrops along the

498   fault zone (S$_{3A}$, S$_{3B}$, W$_{1A}$, W$_{1B}$) is also reported. Black thick lines represent fracture lineaments

499   spatially related to discrete alteration zones. The black dashed lines bracket the supposed maximum

500   width of the damage zone. (b) Geological cross section along the A–A' profile of the Goddo Fault

501   Zone. FC: Fault core; DZ: Damage zone.

502

503
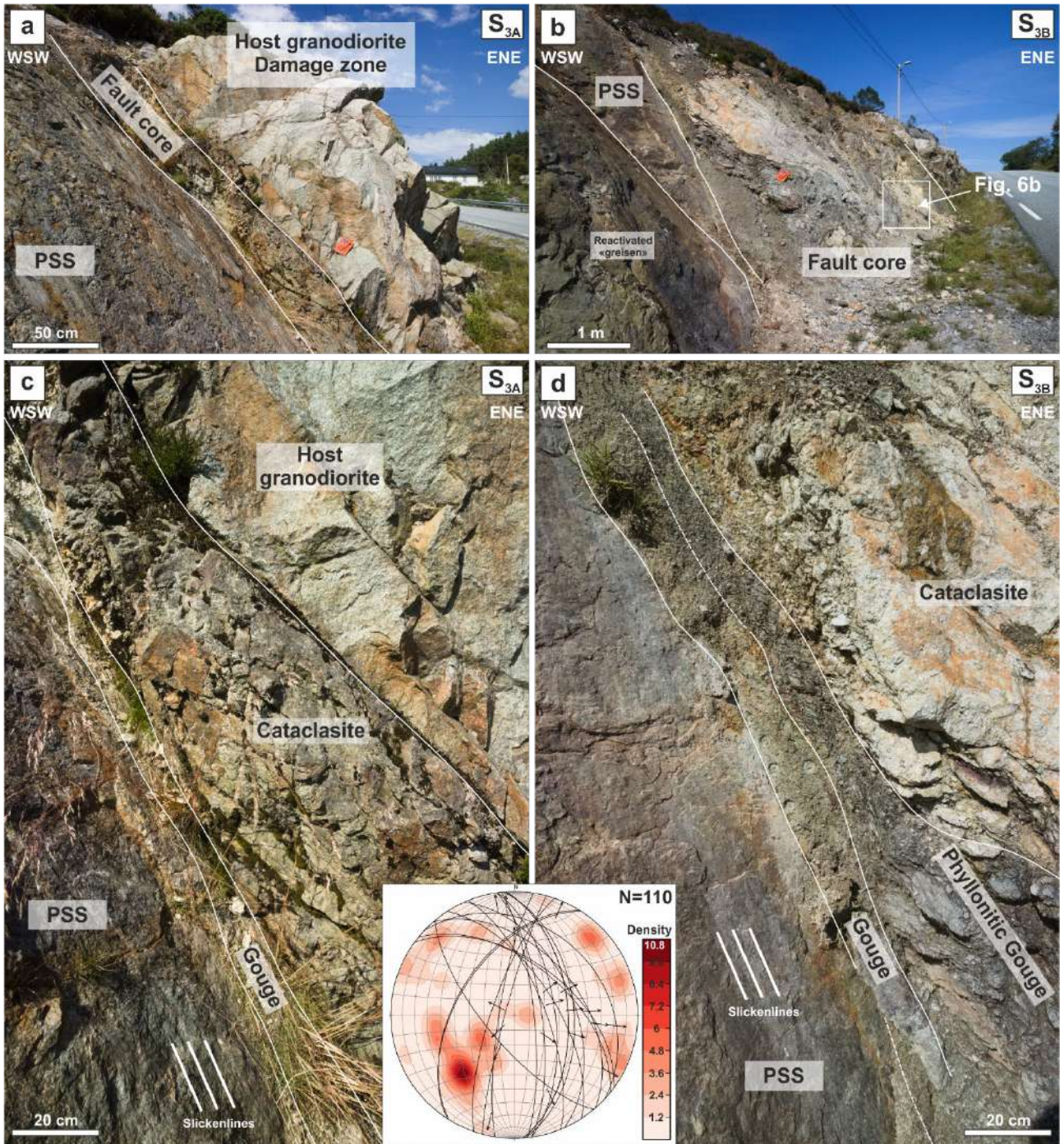
Figure 5: Representative outcrops of the Goddo Fault Zone. (a) Fault core at outcrop S$_{3A}$, showing the composite fault core. (b) Composite fault core and the reactivated slip surface of a "greisen" pre–faulting fracture exposed at S$_{3B}$. (c) Composite fault core at S$_{3A}$, showing the juxtaposition of cataclasite, gouges, and PSS. (d) Composite fault core at S$_{3B}$, showing the juxtaposition of cataclasite, gouge, and PSS. Note the alteration of the cataclasite layers. Stereonets: Lower hemisphere, equal area projection of fractures and fault planes at S$_3$. The whole dataset of fracture and fault planes

510   collected on the field is reported as contoured distribution of poles to fracture and fault planes (in

511   red). Black great circle represent only those fracture and fault planes characterised by slip lines

512   (lineations, slickenlines). The black arrows represent the direction of movement of the hanging wall

513   along the fault plane.

514
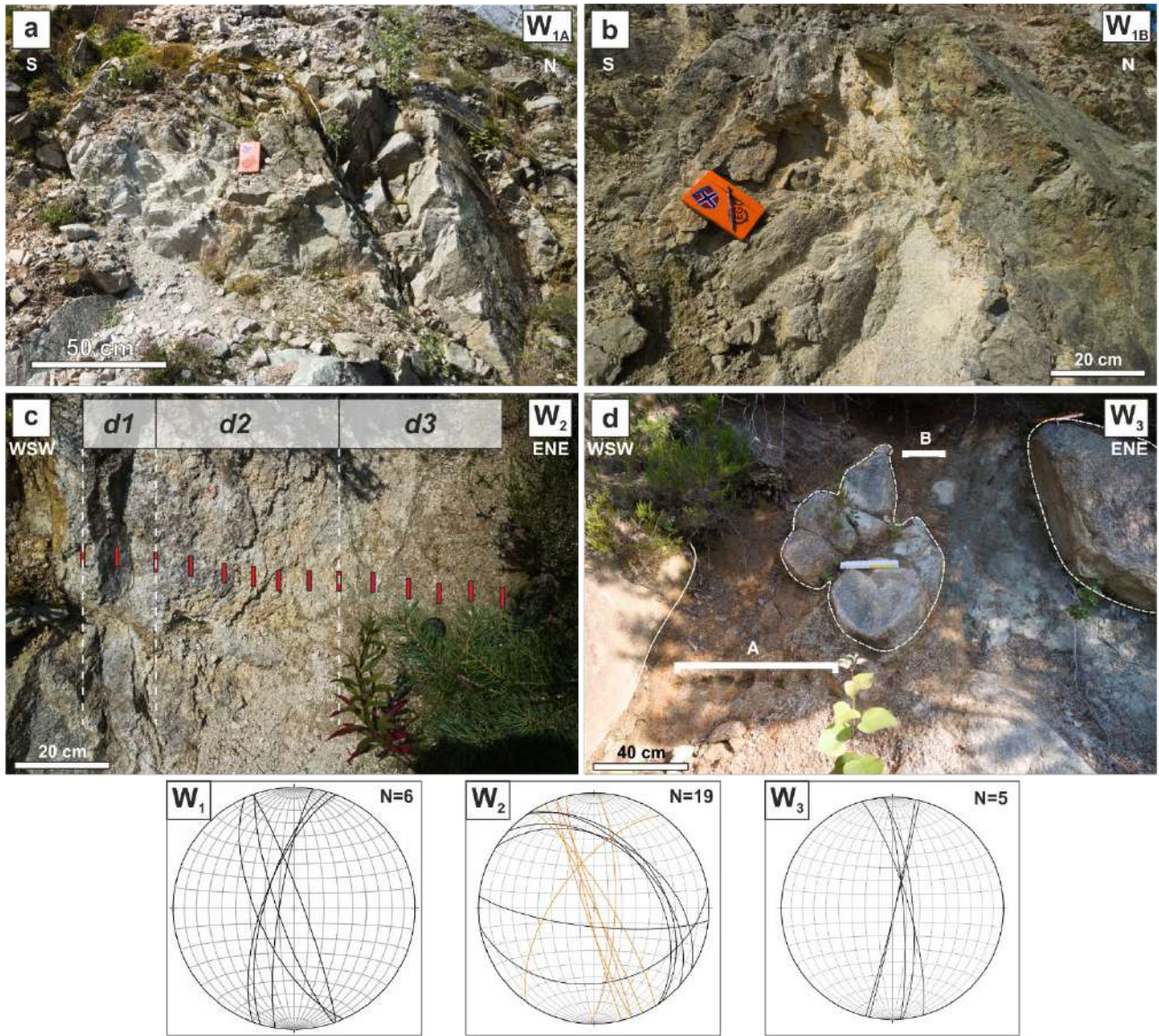
Figure 6: Representative outcrops of weathered granodiorite. (a) Alteration zone W_{1A} related to a NNE–SSW–trending fracture lineament. (b) Alteration of the host granodiorite within the damage zone of the GFZ at W_{1B} (detail of Fig. 5b). (c) Outcrop W_2 showing an increasing alteration profile along which we performed Schmidt hammer analysis and permeability measurements. (d) Outcrop W_3 (saprolite) showing relatively unaltered "core stones" (enclosed by dashed white lines). The thick white lines (A, B) represent the profile along which permeability and UCS measurements have been performed. Stereonets: Lower hemisphere, equal area projection of fracture planes at outcrops W_1, W_2 and W_3. Orientation of fractures within fracture clusters related to weathering zones at outcrop W_2 are highlighted in orange in the stereoplot.

4.2 UCS and permeability data

Data are presented in the following according to rock type (host rock, fault rocks and weathering products) as observed from many different outcrops, to derive an average value and constrain the natural variability range for each lithology. Average values of UCS and related standard deviations are reported in the text and Fig. 7a. Permeability ranges are presented in the text and data distributions are reported as boxplots in Fig. 7b.

4.2.1 Host rock

The RGD on the island of Bømlo still well preserves its magmatic texture and mineralogical composition. No pervasive ductile fabrics have been observed at the analysed outcrops, confirming the observations of Scheiber and Viola (2018). UCS values for the RGD host as observed at three different localities (outcrops S_1–S_2–W_3). Fresh, non–altered and non–mineralised granodiorite surfaces yield an average UCS value of 169 ± 36 MPa. Granodiorite surfaces bounding alteration/weathering zones (measured at outcrops W_2–W_3) exhibit a lower range of UCS variability, with an average value of 107 ± 29 MPa ("Weathered Granodiorite surface" in Fig. 7a). Results from permeability measurements on the pristine, non–fractured host granodiorite at different outcrops range between <10^{-4} D (below the actual reliability limit of the air–minipermeameter) and 0.1 D (Fig. 7b).

4.2.2 Outcrop S_1 – SSRS Fracture corridor

UCS measurements are from along a transect perpendicular to fracture strike. In order to evaluate the influence of fracture intensity on the UCS, we have quantified fracture intensity with circular scan windows (10 cm in diameter) centred on each measurement spot along the transect (Fig. 8a) (Watkins et al., 2015). UCS values comparable to fresh and slightly altered host RGD are measured in the outermost portion of the fracture corridor (Fig. 8b–c). Mechanical strength drastically decreases to 15–20 MPa toward the centre of the fracture corridor, where fracture intensity is higher (P_{21} = 74 m$^-$

551 [1]; Fig. 8b–c, e). The permeability is inferred to be related to only meso–scale fracture aperture and

552 interconnectivity. In order to have a relative comparison with the permeability data presented in the

553 next sections, 2D structural permeability at the scale of the outcrop has been evaluated by analysing

554 the digitised fracture network obtained from line drawing on a field photo of the core zone with the

555 software FracPaQ (Healy et al., 2017). During line drawing, only the subvertical fractures were

556 considered for the definition of the fracture network pattern (Fig. 8d). The subhorizontal fractures are

557 likely related to post–tectonic outcrop modifications related to either post–glacial unloading or man–

558 made excavation and blasting operations, given that such fracture orientation is not observed in any

559 other fracture set related to the brittle deformation history of the Bømlo crystalline basement

560 (Scheiber and Viola, 2018). The 2D permeability of the fracture pattern in the direction of flow was

561 calculated considering a range of different values of fracture aperture, ranging from 0.01 to 1 mm and

562 perfect connectivity among fractures. The outcrop–scale maximum permeability is always oriented

563 parallel to the dominant subvertical fractures, and maximum values range between 10^3 D to 10^{-3} D,

564 for a fracture aperture of 1 mm and 0.01 mm, respectively (Fig. 8e).

565

566 *4.2.3 Outcrops S_2–S_3 –Fault rocks*

567 UCS bulk rock data on fault rocks have been measured at the S_2 and S_3 outcrops. The PSS is

568 characterised by high UCS values when analysed normal to the surface (274 ± 32 MPa, Fig. 7a).

569 Permeability measured normal to the slip surface is in the 0.05 to 0.06 D range (Fig. 7b). UCS of the

570 clay–rich gouge layer is 12 ± 2 MPa, measured parallel to fault strike. Gouge layers present a lower

571 range of permeability, between 10^{-3} D and 0.4 D measured parallel to fault strike (Fig. 7b). The rough

572 exposure surface of the phyllonitic gouge facies did not allow us to perform reliable measurements

573 (Fig. 5d). The cataclasite shows strongly anisotropic UCS, as inferred comparing the results obtained

574 from measurements performed parallel (36 ± 22 MPa) and perpendicular (195 ± 37 MPa) to fault

575 strike (Fig. 7a). The cataclastic core presents a variable permeability ranging between 10^{-3} D and 3 D

576 when measured parallel to fault strike (Fig. 7b). The rough exposure surface of the cataclasite did not

577 allow us to perform reliable measurements of permeability perpendicular to fault strike.

578 *4.2.4 Group W_1–W_3. Weathering along fractures and fault zones*

579 **Outcrop W_1.** UCS for altered granodiorite ranges between 30 and 90 MPa ("Weathered

580 Granodiorite" in Fig. 7a). Values larger than 100 MPa are found in the weathered host granodiorite

581 where the alteration is locally less developed. In the fracture corridor, altered granodiorite lithons are

582 surrounded by a fine–grained sandy, rather non–cohesive matrix that exhibits low UCS values (<15

583 MPa) ("loose matrix" in Fig. 7a). The host granodiorite altered lithons exhibit a variable permeability,

584 ranging between 10^{-3} D and 0.84 D (Fig. 7b).

585 **Outcrop W_2.** Outcrop W_2 displays a clear variation of mechanical strength and permeability with

586 increasing weathering grade (Figs. 6c, 9a). Incipient alteration in domain *d1* exhibits variable UCS

587 between 20 and 50 MPa and variable permeability ranging between 10^{-3} D and 1 D. Similar values

588 were measured from the altered RGD observed at outcrop S_2. The cohesionless alteration products in

589 domain *d2*, consisting of a grus–type sandy aggregate, yields UCS values <20 MPa. Permeability

590 increases (from 0.1 D up to several Darcy's) and then decreases (from >1 D down to 0.01–0.1 D)

591 moving from the left–hand side boundary to domain *d1* toward the right–hand side boundary to

592 domain *d3* (Figs. 6c, 9a). Alteration domain *d3* is characterised by variable UCS < 20 MPa, and low

593 permeability (from 0.01–0.1 D down to few mD).

594 **Outcrop W_3.** Partially weathered "core stones" exhibit a broad range of UCS values, ranging between

595 75 MPa and 125 MPa (Fig. 7a). They have a permeability included between 0.01 D and 0.1 D (Fig.

596 7b). The clay–rich saprolite volume has been analysed along two transects (Fig. 6d). Both transects

597 yield almost constant UCS and permeability values within the clay–rich saprolite (UCS = 10–15 MPa,

598 k = 10^{-2}–10^{-3} D) (Fig. 9b).

599

600

601
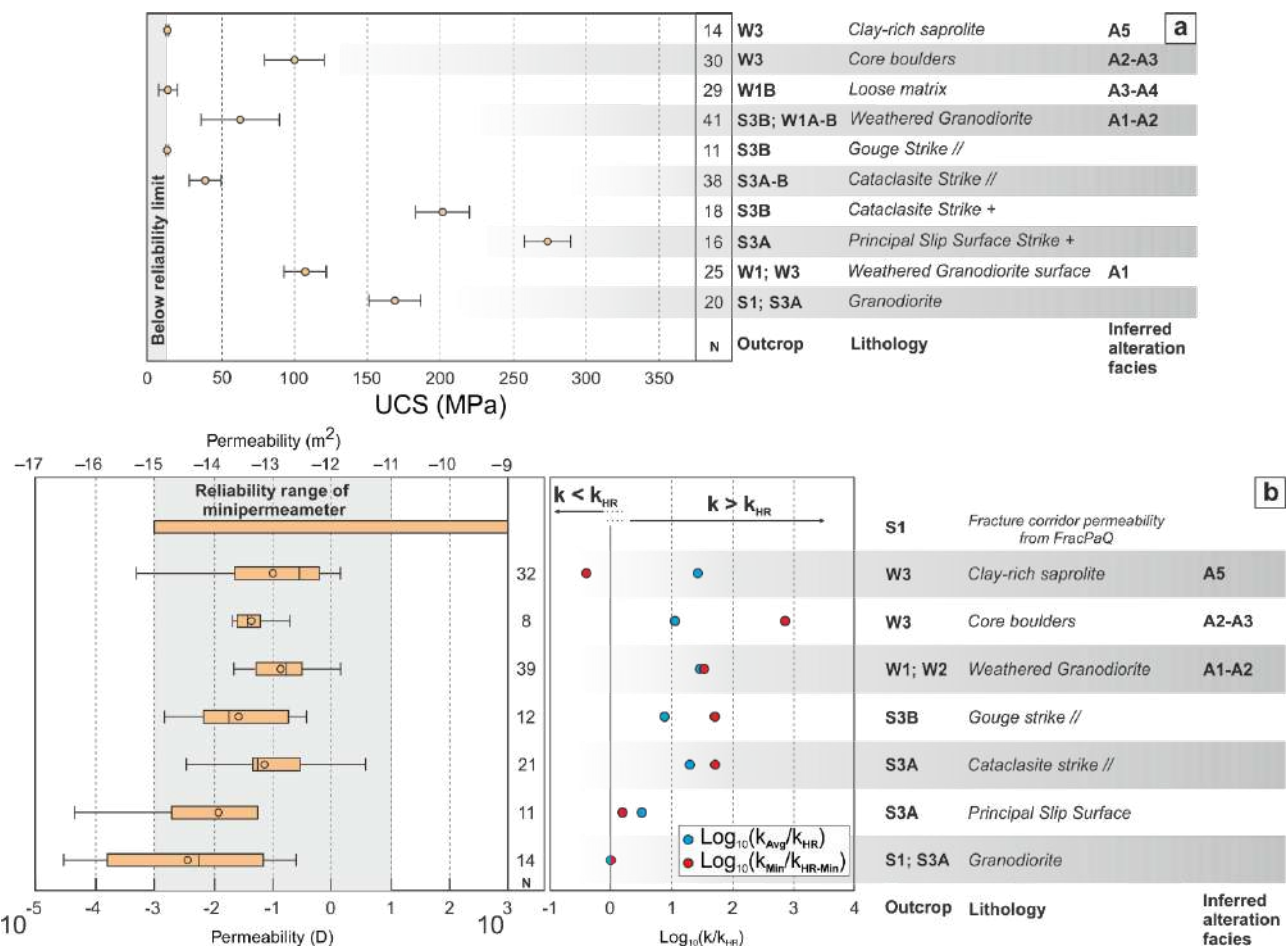
Figure 7: Mechanical strength and permeability box–plot diagrams. "Strike //" stands for data measured parallel to the fault plane. "Strike + " stands for data measured perpendicular to the fault plane. (a) Uniaxial Compressive Strength (UCS, MPa). For each analysed lithology we report the mean (orange dot), the standard deviation (1σ, black bars), the number of measurements (N), the outcrop(s) name on which the measurements were performed, and the corresponding alteration facies. (b) Permeability (m^2, D). The outcrop name and the corresponding alteration facies are reported. N: number of measurements for each lithology. Each box of the box–and–whiskers plot represents the range between the 1st and 3rd quartile of the distribution. The whole data range is represented by the extension of the whiskers. In (b) we also plot the logarithm of the permeability ratio ($Log_{10}(k/k_{HR})$) between the host rock and the selected lithology (Scibek, 2020). The ratio between mean values of permeability (blue dots) and the ratio between the minimum reported values (red dots) for each

36

613   lithology are also reported. It is worth noting that air–minipermeametry retrieved permeability values

614   for saprolites are comparable to those obtained from laboratory measurements on saprolite samples

615   from Bømlo and the Utsira High exploration wells (Lothe et al., 2018).

616
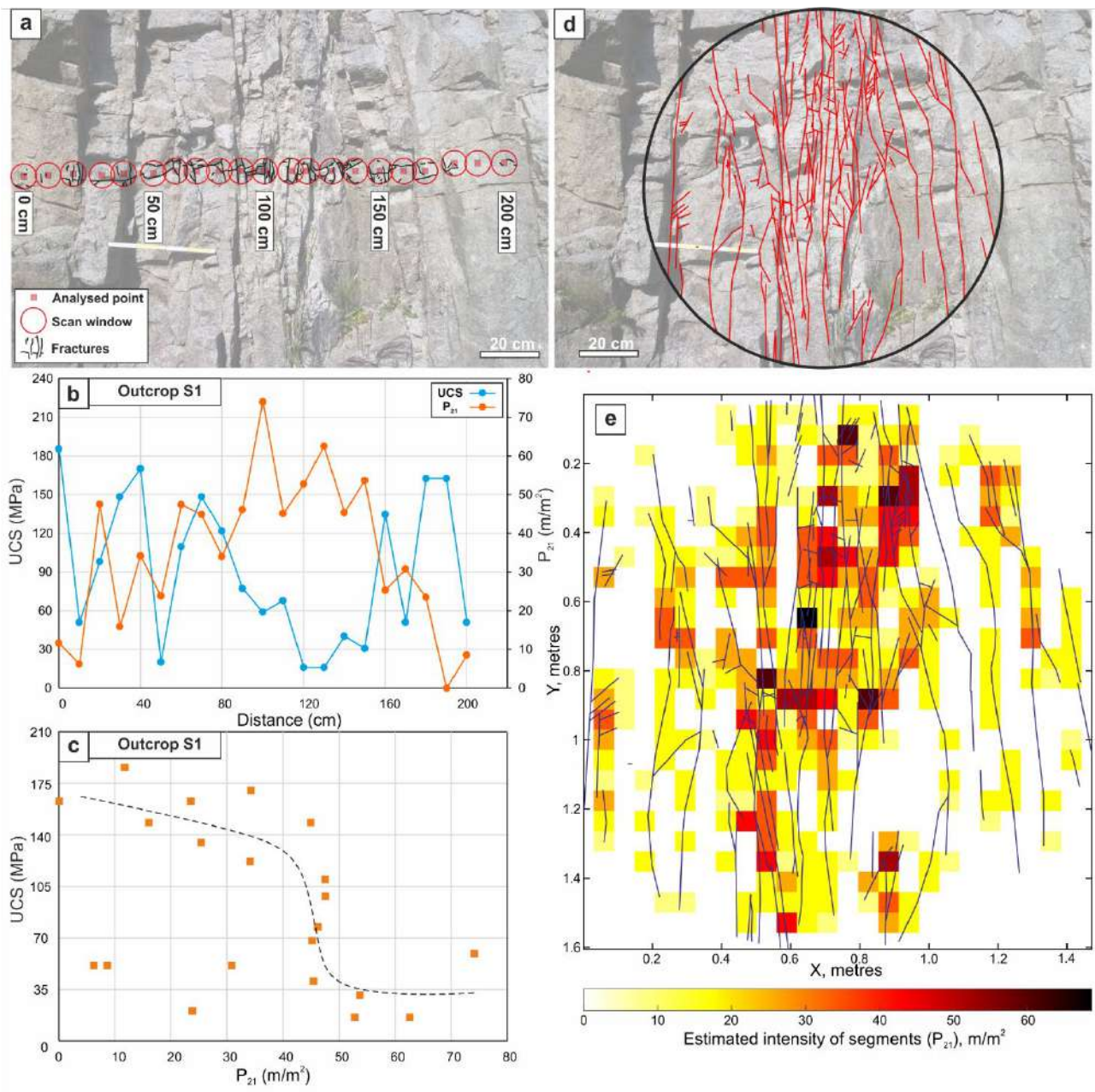
Figure 8: Results of the geomechanical and permeability measurements at outcrop S_1. (a) Location of the measurements for the Schmidt hammer analysis, and circular scan windows for fracture intensity P_{21} quantification; (b) Variation of mechanical strength (UCS) and fracture intensity (P_{21}) along the analysed transect. (c) UCS against fracture intensity P_{21}. Note the drastic decrease of mechanical strength after a threshold value of P_{21} at about 45 m^{-1}. (d) Line drawing of the subvertical fracture network analysed with FracPaQ (Healy et al., 2017); (e) Results of 2D permeability and fracture intensity quantification from FracPaQ..

Figure 9: Results of mechanical strength and permeability quantification along the transect at outcrops (a) W_2 and (b) W_3. Letters A and B in (b) refer to the two transects shown in Fig. 6d.

631   5. **Discussion**

632   We have characterised the structural and weathering features controlling the matrix permeability and

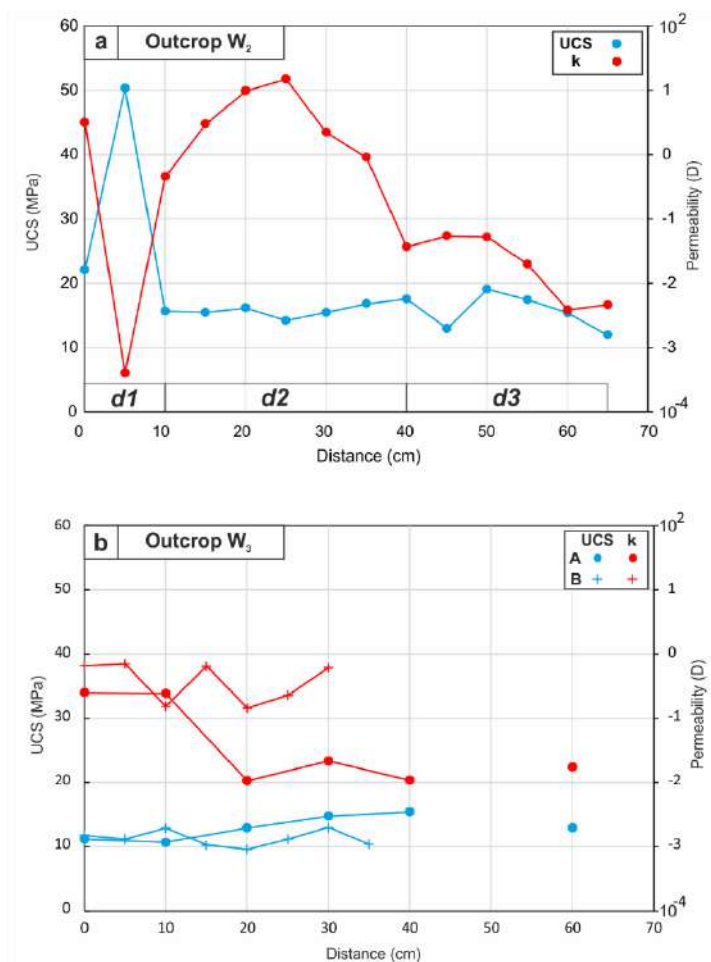633   mechanical properties of the fractured and altered crystalline basement at a number of representative

634   outcrops. In the following paragraphs we discuss (i) the host rock properties, (ii) the matrix

635   permeability related to SSRS and SRS deformation zones, (iii) the mechanical strength and

636   permeability related to weathering products, and (iv) their bearings on the definition of reservoir rock

637   in crystalline basement structural highs.

638   The data presented in this paper represent the present–day, actual mechanical strength and

639   permeability at surficial, ambient conditions. The extrapolation of these values to depth (at deeper

640   structural levels or buried below a sedimentary cover) needs to take into consideration the effect of

641   increasing confining pressure and temperature and the compaction processes (Rutqvist and

642   Stephansson, 2003; Faulkner, 2004; Faulkner et al., 2006; Lothe et al., 2018). A further complication

643   arises from the fact that the analysed onshore outcrops may have been affected by renewed alteration

644   related to Cenozoic geomorphic and glaciogenic processes, which the fractured and weathered

645   crystalline basement buried in the North Sea by the Mesozoic cover has, instead, probably escaped.

646   The petrophysical and mechanical data presented here, however, are comparable (on average) with

647   other results in the literature from standardised laboratory tests on fresh samples from onshore

648   outcrops and offshore core samples of the same rock types analysed here (Lothe et al., 2018; Walter

649   et al., 2018; Høien et al., 2019). This suggests that possible Cenozoic geomorphic and glaciogenic

650   processes have only slightly affected the textural, mechanical and petrophysical characteristics of the

651   studied onshore outcrops.

652   *5.1 Host rock properties*

653   The observed host granodiorite UCS is comparable to the reference values reported in the database

654   by SINTEF for Norwegian rock types (Høien et al., 2019). Permeability data from the RGD are quite

655   different from available laboratory permeability measurements on intact rocks (Sibson and Rowland,

656 2003). Most of the host rock permeability values are comparable with permeability values obtained

657 from fractured crystalline and igneous rock in fault damage zones (Forster and Evans, 1991; Evans

658 et al., 1997; Cappa and Rutqvist, 2011; Gomila et al., 2016). This discrepancy might be related to

659 either: (i) an analytical error during measurement (i.e. air slippage from the non–perfectly sealed

660 contact between the probe tip and the rough surface); (ii) enhanced permeability related to the

661 increased microfracture density in the proximity of fracture and fault zones (Mitchell and Faulkner,

662 2012; Belaidi et al., 2018; Torabi et al., 2018; Staněk and Géraud, 2019); (iii) enhanced permeability

663 related to recent, very local surficial weathering processes. Therefore, further investigations are

664 needed to properly constrain the permeability of the host RGD.

665 *5.2 Group S –Mechanical strength and permeability of deformation zones*

666 The host crystalline basement (RGD) is overprinted by several sets of fractures, including fracture

667 corridors and SSRS–SRS fault zones (Gabrielsen and Braathen, 2014; Scheiber and Viola, 2018).

668 These fracture lineaments affect differently the mechanical and permeability properties of the host

669 RGD and thus require a separate discussion.

670   *5.2.1 SSRS fracture corridors*

671 Fracture corridors are characterised by high–fracture–intensity deformation zones, accommodating

672 limited (< 1m) throw, mostly barren of fault rock. The outcrop mechanical strength and bulk

673 permeability are mainly controlled by the spatial distribution of meso–scale fractures (Fig. 8c, e).The

674 increase in local fracture intensity leads to a drastic decrease of the host rock mechanical strength for

675 $P_{21} > 40$–50 m/m^2 (Fig. 8b–c). High fracture intensity leads to a significant increase of fracture

676 permeability up to 1–10^3 D (Fig. 7b). The largest 2D permeability in the direction of flow is observed

677 parallel to the longer, subvertical and well interconnected fractures (Fig. 8e). Such a fracture network

678 represents a preferential pathway for fluid flow (Souque et al., 2019). Thus, the permeability of

679 limited–throw SSRS fracture corridors is controlled by the mesoscopic fracture porosity. On the other

680 hand, microscopic fracture porosity may contribute to the matrix mechanical strength and

41

681   permeability to only a very limited extent (Faulkner et al., 2006; Mitchell and Faulkner, 2012; Rempe

682   et al., 2018). A local increase in permeability related to microscopic fracture porosity is reported by

683   Torabi et al. (2018) for fracture corridors developed within the Øygarden Gneiss Complex in the

684   Bergen area. Therefore, such SSRS, limited–throw fractures remarkably affect both the overall

685   mechanical and permeability properties of the crystalline basement.

686   *5.2.2 SSRS and SRS fault cores*

687   Strain accommodation and development of fault rocks along SSRS–SRS fault zones resulted in a

688   drastic modification of textural, mechanical and petrophysical properties of the host RGD. Fault

689   zones, either SSRS or SRS, are characterised by the development of a variably thick fault core,

690   defined by the occurrence of fault rocks, and a variably developed damage zone (Caine et al., 1996).

691   SSRS fault cores are likely to be characterised by thin, single fault cores (< 1m thickness) surrounded

692   by poorly developed damage zones (e.g., outcrop S_2). SRS fault zones, instead, may be characterised

693   by the occurrence of thicker (≥ 1 m), multi–strand fault cores surrounded by complex, thick and high–

694   fracture–intensity damage zones (Walsh et al., 1999; Gabrielsen and Braathen, 2014).

695   In both SSRS and SRS fault zones, the fault core is characterised by a composite fault plane–parallel

696   sequence of fault rocks including a PSS, cataclasite, and potentially (several) gouge layers. Extreme

697   strain localisation and rock comminution resulted in the formation of a thin, yet mechanically strong,

698   PSS with a low permeability (Fig. 7a,b). Cataclasite mechanical strength is strongly anisotropic (Fig.

699   7a). Cataclasites are stronger (UCS >> 100 MPa) where measured normal to the fault plane and

700   weaker (UCS <50 MPa) where measured parallel to the fault plane. Cataclasite permeability is up to

701   two orders of magnitude larger than the average permeability of the host rock (Fig. 7b). Gouge layers

702   yield a very–low mechanical strength (UCS < 20 MPa), and low permeability parallel to the fault

703   plane ($k < 10^{-1}$ D). A strong anisotropy in permeability is expected for both cataclasite and gouge

704   layers (up to three orders of magnitude) (Faulkner and Rutter, 1998). The lower strength and increased

705   permeability parallel to the fault plane is probably also related to a higher density of fault–parallel

microfractures and micro–shear planes within cataclasite and gouge layers (Zhang and Tullis, 1998). A pervasive phyllosilicate–bearing foliation characterises the phyllonitic gouge of the GFZ. Thus, even though we lack direct measurements, a strong permeability and strength anisotropy should be expected for the phyllonitic gouge (Shea and Kronenberg, 1993; Niemeijer and Spiers, 2005; Leclère et al., 2015). Cataclasites and gouge layers are in any case two orders of magnitude more permeable that the host RGD (Fig. 7b). Grain–size reduction, cataclasis and microfracturing processes likely led to the increased micro–fracture–related porosity of fault rocks with respect to that of the host granodiorite (Staněk and Géraud, 2019).

5.2.3 Damage zones

The discrete and multi–strand fault cores are surrounded by variably developed fracture–dominated damage zones, whose width is one order of magnitude larger than fault core thickness (Faulkner et al., 2010). The mechanical strength and bulk permeability of the damage zone is strictly dependent on the intensity, mechanical properties and geometry of multi–scale fractures related to both the fault zone and the basement background fracturing (Bruhn et al., 1994; Faulkner et al., 2006; Gudmundsson et al., 2010; Mitchell and Faulkner, 2012; Rempe et al., 2018). Local permeability within the damage zone might be as large as the permeability of similarly high–fracture–intensity fracture corridors (Gabrielsen and Braathen, 2014). An accurate characterisation of the fracture pattern geometry is needed to properly quantify the effect of mesoscopic fractures on the evolution of mechanical properties and bulk permeability in a damage zone (Healy, 2008; Gudmundsson et al., 2010).

In conclusion, SSRS and SRS deformation zones have distinctive structural characteristics controlling their permeability structure. Low–strain, low–displacement SSRS fracture corridors characterised by open, non–mineralised fractures greatly enhance the permeability of the crystalline basement at the sub–seismic–resolution scale. They form very localised, narrow (1–10 m in width) highly–efficient conduits for fluid flow. The largest permeability is observed parallel to the average fracture plane

43

731 orientation. SSRS and SRS fault zones are characterised by two domains with characteristic

732 permeability (Caine et al., 1996; Evans et al., 1997): (i) the fault core, including low–permeability

733 fault rocks; (ii) the damage zone, defined by a high–permeability multiscale fracture network. The

734 permeability of fault rocks and damage zones is in any case several orders of magnitude larger than

735 the host rock. Therefore, despite their effective (SSRS or SRS) or relative (fault core/damage zone

736 width ratio) size characteristics, fault zones developed within the granodioritic crystalline basement

737 of Bømlo are likely to act invariably as preferential conduits for fluid flow. Fluid flow will be

738 promoted in any directions parallel to the fault zone, along the highly fractured damage zones. Fluid

739 flow from footwall to hanging wall of SRS fault zones, or vice versa, might be buffered/limited by

740 the occurrence of relatively low–permeability fault cores.

741 *5.3 Group W outcrops and a comparison with the Utsira High weathering profile*

742 Several authors described in detail the mineralogical and textural changes of the granitoid crystalline

743 basement of the Utsira High related to the development of a saprolitic weathering profile identified

744 in the core samples of offshore exploratory wells (Riber et al., 2015, 2016, 2017, 2019a; Lothe et al.,

745 2018). They describe five different alteration facies accounting for the observed gradual

746 disaggregation of the igneous host rock, the alteration of feldspar, and clay mineral formation. In their

747 model, progressive downward penetration of meteoric fluids from the top–basement surface led to

748 the development of a thick weathering profile containing both saprock and more mature saprolite

749 formed at the expense of the host granitoid (Fig. 2a–b) (Riber et al., 2015, 2019b; Walter et al., 2018;

750 Zauyah et al., 2018). Weathering extends from the top–basement surface (that was exposed to a sub–

751 aerial tropical–humid climate) into depth in the rock column: the progressive degradation of the host

752 rock primary structure and the presence of a pervasive network of fractures and fault zones promoted

753 the penetration at depth of fluids enhancing alteration (Braathen et al., 2018; Walter et al., 2018;

754 Zauyah et al., 2018). The weathering process induces specific textural and mineralogical modification

755 of the host rock. Incipient weathering along fractures leads to discolouring and limited mineral

alteration while still preserving the igneous/metamorphic rock texture ("altered coherent facies A1–A2" in Riber et al., 2016; Fig. 2b). The alteration of biotite and plagioclase leads to progressive grain disaggregation and grain fracturing, clay mineral and Al–Fe oxide formation (saprock – saprolite, "altered incoherent facies A3–A5" in Riber et al., 2016; Fig. 2b) (Goodfellow et al., 2016; Hayes et al., 2019). Progressive weathering is also reflected in a varying mineralogy of authigenic clay minerals, with smectite being progressively substituted by kaolinite as the degree of weathering increases (Coggan et al., 2013; Riber et al., 2016).

A similar transition in mineralogical and textural characteristics of the RGD with increasing alteration can be deduced by the comparison of the preserved weathering remnants at the analysed Group W outcrops. Each outcrop effectively shows different textural, mineralogical (clay–mineral amounts and species), and mechanical characteristics, which indicate progressive weathering and alteration. Outcrops W_1–S_1 only display partial alteration of the wall rock along fractures while preserving the textural and mechanical properties of the host rock. The weathering products are represented by samples BO–OFR–1 (Viola et al., 2016) and TSC–1 (Scheiber and Viola, 2018). The finest–fractions of these samples are enriched in smectite–like phases, suggesting only incipient alteration (Coggan et al., 2013; Riber et al., 2016). The characteristics of this outcrop, thus, resemble those of the "alteration facies A1–A2" described by Riber et al. (2016). The alteration products observed at outcrop W_2 document, instead, a transition from a coherent host rock (domain *d1* in Fig. 6c) toward a cohesionless, sandy, grus–type aggregate preserving the magmatic texture but not the mechanical cohesion of the host rock and increasing clay content (domain *d3* in Fig. 6c). The intermediate alteration domain *d2* at outcrop W_2 presents textural and mechanical characteristics similar to the alteration products observed at outcrop S_2. Sample TSC–36 from outcrop S_2 shows increasing kaolinite content over smectite (Scheiber and Viola, 2018). The clay content and the textural characteristics of domain *d2* at outcrop W_2 and outcrop S_2 are similar to those described for "alteration facies A3–A4" by Riber et al. (2016). The clay–rich alteration product in outcrop W_3 is present in the

781   set of samples analysed by Fredin et al. (2017b) (Bomlo2–3–4). Kaolinite is predominant over

782   smectite–like phases, suggesting an advanced stage of alteration (Coggan et al., 2013; Riber et al.,

783   2016). Outcrop W_3 mineralogical and textural characteristics are similar to the "alteration facies A5"

784   described by Riber et al. (2016).

785   Even though the alteration products analysed in the Group W outcrops may result from diachronic

786   events, they all present textural and mineralogical characteristics which are ascribable to

787   kaolinitisation and/or saprolitisation of the RGD host (Coggan et al., 2013; Riber et al., 2016; Fredin

788   et al., 2017b). Indeed, alteration processes took place at either shallow crustal levels (<6km? depth,

789   Scheiber and Viola, 2018) or surficial conditions (weathering – saprolitisation) (Fredin et al., 2017b).

790   It is worth noting that, in each of the analysed outcrops, the weathering products postdate the

791   formation of brittle structures and are not overprinted by any subsequent brittle deformation. This

792   may suggest that weathering likely developed during periods of quiescent tectonic activity, as it is

793   postulated for the development of thick saprolitic horizons (Fredin et al., 2017b)

794   Therefore, we speculate that the studied Group W outcrops may be adopted as representative of the

795   different stages of progressive weathering. The partially altered outcrop W_1 represents the deepest

796   portions of the weathering profile; the outcrop W_2 represents the intermediate alteration stage and the

797   transition toward more evolved alteration products, which are well represented by outcrop W_3 (Fig.

798   10) (Lothe et al., 2018).

799   Such a defined weathering profile displays a progressive degradation of mechanical strength and an

800   overall permeability enhancement with the increasing weathering grade (from A1 to A5, Fig. 10b).

801   Incipient alteration A1–A2 leads, on average, to a progressive decrease in mechanical strength of

802   about 50% of the intact RGD. The permeability at this stage of weathering is increased up to 0.01–1

803   D. The transition from coherent (A2) to incoherent alteration facies (A3–A5) is characterised by a

804   drastic decrease in mechanical strength (UCS down to < 20 MPa, Fig. 10b). Conversely, the

805　　permeability increases up to 10 D within alteration facies A3–A4, and then progressively decreases

806　　toward 10^{-4} D when approaching alteration facies A5 (Fig. 10b).

807　　The observed variability of the studied properties through the weathering profile is similar to that

808　　commonly reported from saprolitic profiles and alteration profiles related to granite kaolinitisation

809　　(Coggan et al., 2013; Lothe et al., 2018; Walter et al., 2018). In such contexts, the variation of

810　　mechanical strength and permeability are commonly related to the development and evolution of

811　　micro–porosity with increasing weathering (Goodfellow et al., 2016; Lothe et al., 2018; Walter et al.,

812　　2018; Hayes et al., 2019). Microstructural investigations suggest that the petrophysical properties of

813　　incipient alteration stages (coherent alteration facies A1–A2) are controlled by microfracture–related

814　　porosity and biotite alteration (Goodfellow et al., 2016; Walter et al., 2018). The increasing alteration

815　　of biotite and plagioclase into clay–minerals (alteration facies A3–A4) promotes the development of

816　　vacuole–shaped porosity and triggers micro–fracturing as a consequence of positive volume changes

817　　caused by the oxidation reactions in the altering rock (Goodfellow et al., 2016; Walter et al., 2018).

818　　At this stage, highly interconnected pores and micro–fractures enhance the effective permeability and

819　　storage capacity of the weathered rock (Walter et al., 2018). Accordingly, increased micro–porosity

820　　and progressive clay–mineral formation lead to the observed drastic decrease in mechanical strength

821　　between cohesive and cohesionless alteration facies, similarly to what reported by Coggan et al.

822　　(2013) during progressive granite kaolinitisation. The most advanced stages of weathering (alteration

823　　facies A5) are characterised by the complete alteration of biotite and plagioclase into clay–minerals

824　　and Fe–oxides. At this stage, mineral alteration and neoblastesis lead to obstruction of the previously

825　　developed micro–porosity and to the observed reduction of permeability (Walter et al., 2018). As a

826　　result, weathering leads to immediate and drastic decrease of mechanical strength, whereas

827　　permeability firstly increases and then decreases during weathering process progression (Fig. 10).

828　　The characteristics of the weathering profile studied here have three main important implications for

829　　the characterization of reservoir rocks buried offshore beneath the sedimentary cover in the North

830　　Sea structural highs.

831　　(i)　　Weathering around fracture zones, progressive matrix disaggregation, homogenization,

832　　　　　　and the resulting blurring of the structural discontinuities drive the transition from

833　　　　　　structurally controlled permeability of the intact host rock toward the matrix–controlled

834　　　　　　permeability of intermediate alteration facies (Fig. 10). Fracture zones are characterised

835　　　　　　by high permeability, which is, however, spatially confined to the mesoscopic fracture

836　　　　　　porosity and fracture aperture. The highly permeable alteration facies A3 is two orders of

837　　　　　　magnitude less permeable than the maximum permeability inferred for fracture corridors

838　　　　　　(with a fracture aperture of 1 mm). However, it involves larger volumes of the host rock,

839　　　　　　and thus dramatically increases the storage capacity of the reservoir rocks.

840　　(ii)　　The low permeability of alteration facies A5 (saprolite) suggests that the top layers of the

841　　　　　　weathering profile, when preserved, may act as a partial seal to fluid flow at the base of

842　　　　　　the sedimentary cover atop the basement structural highs (Dewandel et al., 2006; Walter

843　　　　　　et al., 2018).

844　　(iii)　　The analysed paleo–weathering profile developed during the Mesozoic, and was then

845　　　　　　buried below the Jurassic–Cretaceous sedimentary succession of the central North Sea.

846　　　　　　The observed differential mechanical strength may have led to different compaction

847　　　　　　patterns and behaviours, and thus a differential modification of the permeability of

848　　　　　　weathering products during the burial history of the paleo–weathering profile (Lothe et

849　　　　　　al., 2018). The weaker clay–rich saprolites may have undergone to a significant change of

850　　　　　　the original secondary porosity and permeability when compared to the more stiff,

851　　　　　　granular saprock and incipient alteration facies (Lothe et al., 2018; Walter et al., 2018).
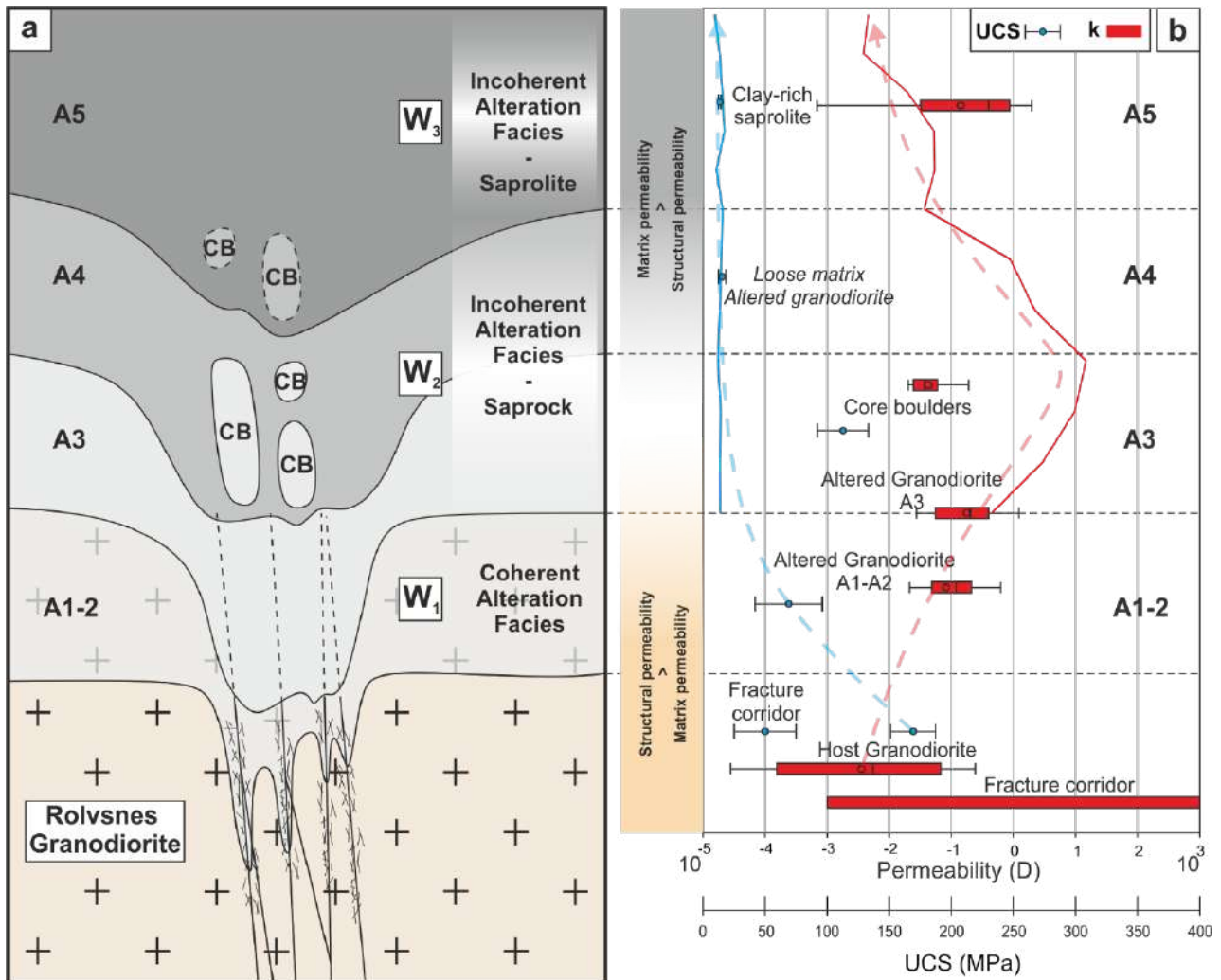
852

Figure 10: (a) Schematic representation of the top–basement weathering profile. The penetration of weathering processes into the crystalline basement is promoted by the structural discontinuities, such as SSRS fractures and fault zones. Alteration intensity decreases with depth. With increasing alteration, structural permeability is progressively replaced by matrix permeability related to the alteration products. (b) Mechanical strength and permeability variations through the alteration profile. The continuous red and light blue curves represent the mechanical strength and permeability observed at W_2. The dashed red and blue curves represent the overall general trend of variation of k and UCS, respectively, through the weathering profile. An initial permeability increment in the deepest portion of the alteration profile is superseded by a drastic permeability decrement toward the more evolved weathering stages.

49

5.4 Reservoir rocks in fractured and weathered basement

The reservoir rocks in fractured and weathered crystalline basement are made up of (Braathen et al., 2018): (1) the fractures and fault (damage) zones within the non–weathered crystalline basement, in which permeability is structurally controlled (Figs. 11, 12), and (2) the products of weathering and alteration, such as the overlying top–basement paleo–weathering profile where the permeability is dominated by the matrix properties of the weathered products (Figs. 10, 12).

The crystalline basement is characterised by the occurrence of a complex network of variably oriented brittle deformation zones (Gabrielsen and Braathen, 2014; Scheiber and Viola, 2018). Fracture corridors and damage zones related to both SSRS and SRS fault zones represent high–permeability conduits for fluid flow (Fig. 11a). The volume of the fractured reservoir suited for fluid storage is therefore limited to the overall deformation zone volume. However, the occurrence of fault rocks within SSRS and SRS fault cores may limit the migration of fluids between highly permeable footwall and hanging wall damage zones. In addition, the intersection of variably oriented fault zones may limit the overall lateral fluid flow through the large–scale network of SSRS–SRS fracture lineaments. This would lead to the formation of fault bounded polyhedral domains (i.e. "reservoir compartments") of the fractured crystalline basement (Fig. 11b) (Watkins et al., 2018). Within each domain, fluid flow is limited to the high permeability fracture corridors and footwall/hanging wall damage zone connected to the domain bounding faults (Fig. 11b).

The reservoir storage volume is likely increased within the top–basement weathering profile and fracture–related alteration zones. Weathering may lead to the formation of very thick (up to 100 meter thick) profiles characterised by high porosity and permeability (Braathen et al., 2018; Walter et al., 2018) (Fig. 12). In addition, fluid percolation through fracture zones may lead to the deep penetration of weathering processes, down to even 300 m below the top–basement paleo surface (Place et al., 2016; Walter et al., 2018). Furthermore, the most altered A5 facies may represent a top–seal layer to

889   the underlying weathered and fractured basement high, buffering the upward migration of fluids

890   toward the overlying sedimentary succession (Figs. 10, 12) (Walter et al., 2018).

891   *5.5 Mechanical strength of fractured and weathered crystalline basement*

892   The fractured and weathered unconventional reservoir under consideration is thus composed of

893   several structural and textural elements with strikingly different mechanical strength. The fracture

894   network and the spatial distribution of weathering/alteration products lead to a significant mechanical

895   heterogeneity/anisotropy within the crystalline basement. In turn, this mechanical heterogeneity and

896   anisotropy may in places significantly perturb the regional stress field (Gudmundsson et al., 2010).

897   This could lead to the relevant modification of the overall fracture network geometry, fracture

898   orientation and spacing within the mechanically heterogeneous rock volume during both natural

899   deformation and induced fracturing of the reservoir (Jeanne et al., 2013; Smart et al., 2014). The

900   occurrence of mechanically weak layers, such as the top–basement weathering profile, the gouge–

901   bearing fault cores, and the partially altered fracture corridors within the crystalline basement may

902   control the orientation and propagation of natural or induced fractures during either tectonic

903   deformation or reservoir production (Douma et al., 2019; Forbes Inskip et al., 2020). In particular,

904   the occurrence of these low–mechanical strength layers and localised heterogeneities may arrest the

905   propagation of fractures artificially induced during the exploitation phase of unconventional

906   reservoirs to enhance the local structural permeability of the host low–permeability crystalline rocks

907   and stimulate production (Forbes Inskip et al., 2020).

908

909

910
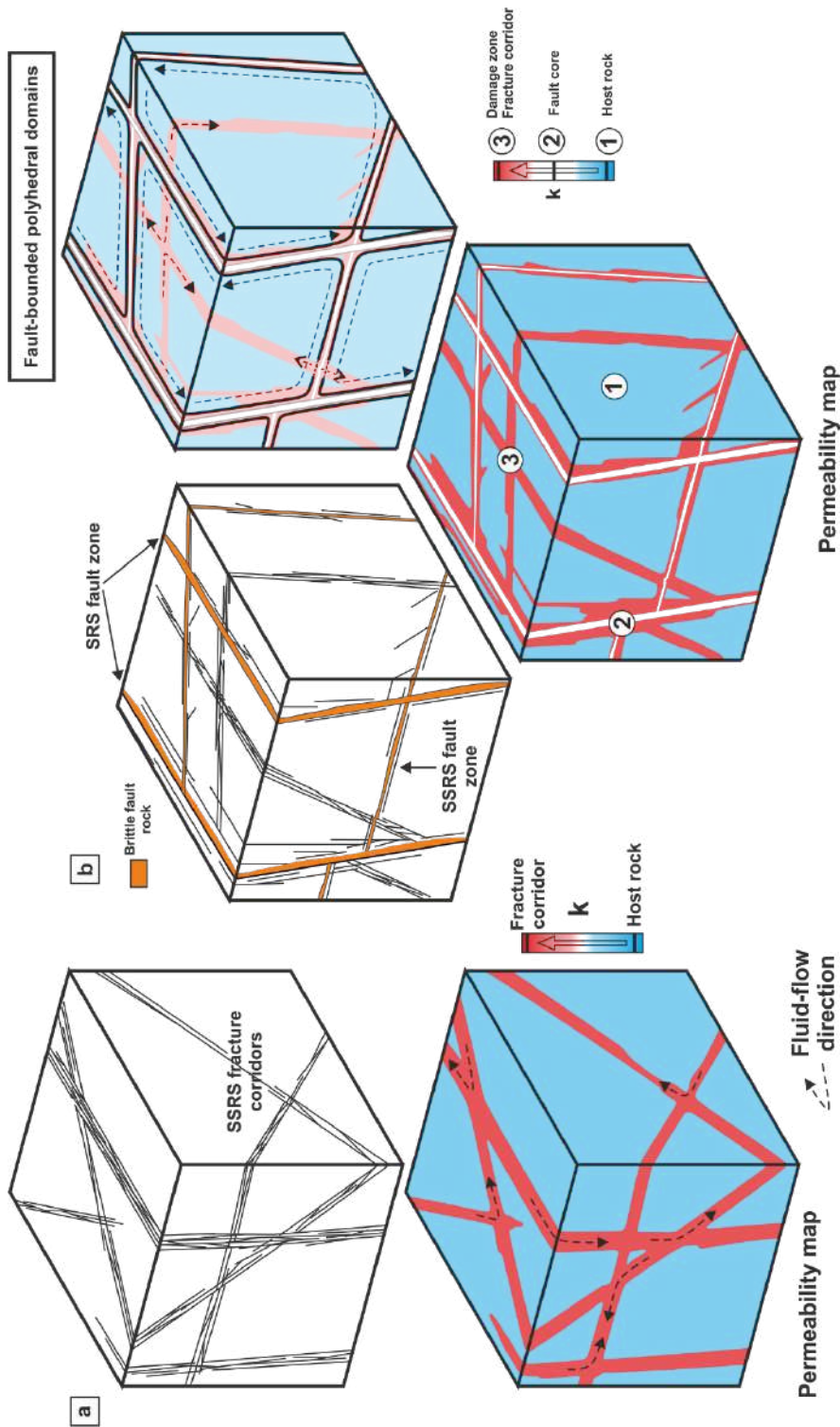
Figure 11: Schematic representation of the conceptualised fractured basement reservoir. (a) Low–strain fracture corridors lead to the development of a high–permeability network of fracture lineaments, dominated by the structural permeability. The randomly oriented dashed arrows in the coloured permeability map indicate the lack of reservoir compartmentalization. (b) The development

915   of sub–seismic–resolution scale (SSRS) and seismic–resolution scale (SRS) fault zones, and related

916   fault rocks within fault cores lead to the development of local low–permeability barriers to fluid flow.

917   The large–scale fracture network is then "compartmentalised" into polyhedral fault–bounded

918   domains, whose dimension depend on the geometry of the fault zone network. Dashed arrows

919   describe a closed path for fluid flow within each fault–bounded domain.
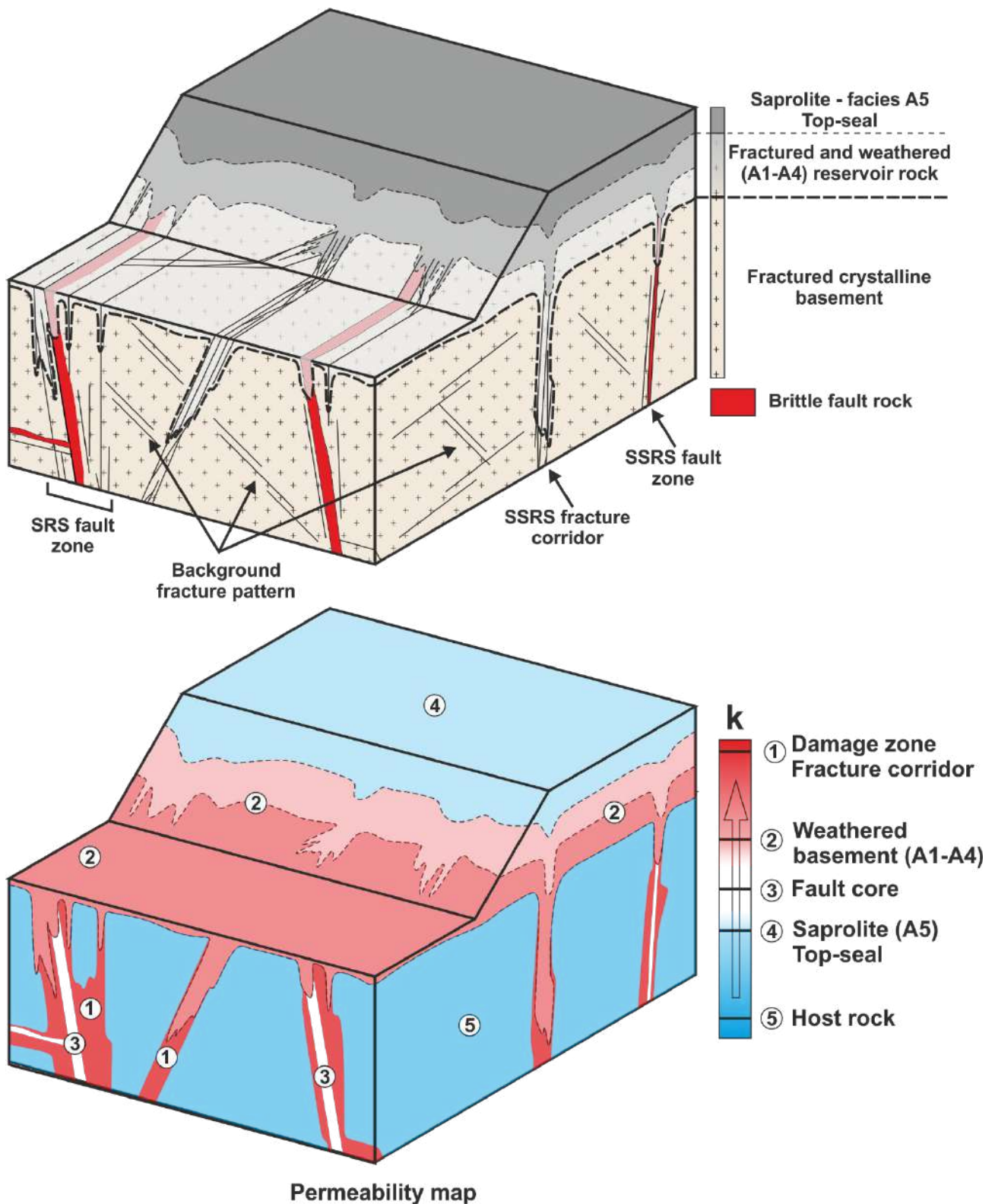
Figure 12. Block diagram summarising a conceptualised model of reservoir within fractured and weathered crystalline basement (not to scale). (a) The top–basement weathering profile overprints the fractured crystalline basement, exploiting the network of fractures and fault zones to penetrate to even great depth (down to to 300 m, Walter et al., 2018). (b) Schematic permeability map of the

925   conceptualised model described in (a). The reservoir is deformed by highly permeable fractures and

926   fault zones (1) and contains the deepest portion of the weathering profile (2). Fault cores (3) are

927   inherently more permeable than the unaltered host rock, thus acting as a conduit for fluid flow parallel

928   to fault strike. The potential reservoir rocks (1–2) and potential fluid conduits (1 and 3) are overlain

929   by the low permeability saprolitic horizon (4), which may act as top–seal layer. Weathering processes

930   greatly increase the fluid storage and transport potential of the reservoir close to the top–basement

931   surface, which is otherwise limited to the network of fractures and fault zones.

932

933

934

6. Conclusion

The matrix mechanical properties and permeability constrained by this study within the crystalline basement rocks exposed on Bømlo result from the prolonged and complex interplay between tectonics and lithosphere–atmosphere interactions (Fredin et al., 2017b). Brittle fracturing and weathering led to the development of secondary porosity at different scales: (a) meso–scale fracture porosity; (b) micro–porosity related to cataclastic processes and micro–fracturing; (c) micro–porosity related to mineral alteration and reaction–induced micro–fracturing. Thus, fault rock formation and weathering processes related to subaerial exposure and fluid percolation through deformation zones deeply affected both the mechanical strength and the matrix permeability of the RGD.

The fractured and weathered crystalline basement reservoir rocks are, therefore, composed of two main constituent elements: (1) the fractured crystalline basement and (2) the weathered/altered rock volume. The multiscale fracture network is composed of different types of fracture zones (SSRS fracture corridor, SSRS and SRS fault zones). Fault zones, either SSRS or SRS, represent zones of enhanced permeability with respect to the host crystalline basement and conduits for fluid flow parallel to the fault planes at all stages of evolution and at all scales (Caine et al. 1996). Meso–scale fractures spatially related to low strain and limited throw fracture corridors drastically enhance the overall permeability of the basement. Similarly, the formation of fault rocks, which are on average two orders of magnitude more permeable than the host rock, significantly increases the crystalline basement matrix permeability. They are characterised by anisotropic mechanical and permeability properties. In addition, they may act as partial seal/buffer layers to fluid flow within the high permeability structural network defined by fracture corridors and damage zones (Bruhn et al., 1994; Caine et al., 1996).

The comparison of weathering characteristics between different outcrops has allowed us to quantify the mechanical strength and permeability as a function of the actual position within the reconstructed

959 weathering profile (Dewandel et al., 2006; Lothe et al., 2018). The weathering profile shows a

960 progressive degradation of mechanical strength coupled to an initial increase in permeability during

961 the incipient stages of weathering (up to 10 D, corresponding to its deepest portion), followed toward

962 shallower depth by a significant decrease in permeability toward the more evolved weathering stages

963 (down to 10^{-3} D). The matrix secondary permeability created during weathering greatly increases

964 fluid storage and migration in a potential reservoir, which would otherwise be limited to volumes

965 with sufficient structural permeability. Mature saprolitic horizons, on the other hand, may act as top–

966 seal layer to the underlying permeable weathered products. As a consequence, weathering profiles

967 may act both as reservoir and top–seal unit in sub–unconformity unconventional reservoirs (Braathen

968 et al., 2018; Holdsworth et al., 2020; McCaffrey et al., 2020).

969 Fractured and weathered crystalline basement reservoirs are characterized by a significant mechanical

970 heterogeneity, as inferred by the strikingly different mechanical properties of deformation zones,

971 brittle fault rocks and weathering products. The mechanical heterogeneity is particularly developed

972 toward the top–basement unconformity, where brittle deformation zones may be decorated by

973 alteration products and abut the overlying weathering profile. The detailed quantification of the

974 mechanical heterogeneity and its spatial distribution is therefore fundamental to optimize the planning

975 strategies for the exploration and the operative exploitation of sub–unconformity unconventional

976 reservoirs.

977

978

988

989

990

991   **References**

992   Armitage, P.J., Faulkner, D.R., Worden, R.H., 2013. Caprock corrosion. Nature Geoscience 6, 79–

993   80. https://doi.org/10.1038/ngeo1716

994   Aydin, A., 2009. ISRM Suggested method for determination of the Schmidt hammer rebound

995   hardness: Revised version. International Journal of Rock Mechanics and Mining Sciences 46,

996   627–634. https://doi.org/10.1016/j.ijrmms.2008.01.020

997   Aydin, A., Basu, A., 2005. The Schmidt hammer in rock material characterization. Engineering

998   Geology 81, 1–14. https://doi.org/10.1016/j.enggeo.2005.06.006

999   Banks, G., Bernstein, S., Salehi, S., Guarnieri, P., Bird, D., Hamblett, C., Peacock, D., Foster, J.,

1000   2019. Liverpool land basement high, Greenland: Visualising inputs for fractured crystalline

1001   basement reservoir models. Geological Survey of Denmark and Greenland Bulletin 43.

1002   https://doi.org/10.34194/GEUSB-201943-02-04

1003   Belaidi, A., Bonter, D.A., Slightam, C., Trice, R.C., 2018. The Lancaster Field: Progress in opening

1004   the UK's fractured basement play. Petroleum Geology Conference Proceedings 8, 385–398.

1005   https://doi.org/10.1144/PGC8.20

1006   Bell, R.E., Jackson, C.A.L., Whipp, P.S., Clements, B., 2014. Strain migration during multiphase

1007   extension: Observations from the northern North Sea. Tectonics 33, 1936–1963.

1008   https://doi.org/10.1002/2014TC003551

1009   Bonter, D.A., Trice, R., 2019. An integrated approach for fractured basement characterization: The

1010   lancaster field, a case study in the UK. Petroleum Geoscience 25, 400–414.

1011   https://doi.org/10.1144/petgeo2018-152

1012   Braathen, A., Abdel Fattah, M.M., Olaussen, S., Abdel-Gawad, G., Ogata, K., 2018. Basement-cover

1013   reservoir analogue in rift-margin fault blocks; Gulf of Suez Rift, Sinai, Egypt. Petroleum

1014   Geoscience. https://doi.org/10.1144/petgeo2016-163

1015   Brace, W.F., 1984. Permeability of Crystalline Rocks: New in Situ Measurements. Journal of

1016   Geophysical Research 89, 4327–4330. https://doi.org/10.1029/jb089ib06p04327

1017   Bruhn, R.L., Parry, W.T., Yonkee, W.A., Thompson, T., 1994. Fracturing and hydrothermal

1018   alteration in normal fault zones. Pure and Applied Geophysics PAGEOPH 142, 609–644.

1019   https://doi.org/10.1007/BF00876057

1020   Caine, J.S., Evans, J.P., Forster, C.B., 1996. Fault zone architecture and permeability structure.

1021   Geology   24,   1025–1028.   https://doi.org/10.1130/0091-

1022   7613(1996)024<1025:FZAAPS>2.3.CO;2

1023   Cappa, F., Rutqvist, J., 2011. Modeling of coupled deformation and permeability evolution during

1024   fault reactivation induced by deep underground injection of CO2. International Journal of

1025   Greenhouse Gas Control 5, 336–346. https://doi.org/10.1016/j.ijggc.2010.08.005

1026   Coggan, J.S., Stead, D., Howe, J.H., Faulks, C.I., 2013. Mineralogical controls on the engineering

1027   behavior of hydrothermally altered granites under uniaxial compression. Engineering Geology

1028   160, 89–102. https://doi.org/10.1016/j.enggeo.2013.04.001

1029   Damsleth, E., Sangolt, V., Aamodt, G., 1998. Sub-seismic Faults Can Seriously Affect Fluid Flow in

1030   the Njord Field off Western Norway - A Stochastic Fault Modeling Case Study., SPE Annual

1031   Technical Conference and Exhibition. https://doi.org/10.2118/49024-MS

1032   Demirdag, S., Yavuz, H., Altindag, R., 2009. The effect of sample size on Schmidt rebound hardness

1033   value of rocks. International Journal of Rock Mechanics and Mining Sciences 46, 725–730.

1034   https://doi.org/10.1016/j.ijrmms.2008.09.004

1035   Dewandel, B., Lachassagne, P., Wyns, R., Maréchal, J.C., Krishnamurthy, N.S., 2006. A generalized

1036   3-D geological and hydrogeological conceptual model of granite aquifers controlled by single

1037   or   multiphase   weathering.   Journal   of   Hydrology   330,   260–284.

1038   https://doi.org/10.1016/j.jhydrol.2006.03.026

1039   Douma, L.A.N.R., Regelink, J.A., Bertotti, G., Boersma, Q.D., Barnhoorn, A., 2019. The mechanical

1040   contrast between layers controls fracture containment in layered rocks. Journal of Structural

1041   Geology 127, 103856. https://doi.org/10.1016/j.jsg.2019.06.015

1042   Evans, J.P., Forster, C.B., Goddard, J. V., 1997. Permeability of fault-related rocks, and implications

1043   for hydraulic structure of fault zones. Journal of Structural Geology 19, 1393–1404.

1044   https://doi.org/10.1016/S0191-8141(97)00057-6

1045   Faulkner, D.R., 2004. A model for the variation in permeability of clay-bearing fault gouge with

1046   depth   in   the   brittle   crust.   Geophysical   Research   Letters   31.

1047   https://doi.org/10.1029/2004GL020736

1048   Faulkner, D.R., Jackson, C.A.L., Lunn, R.J., Schlische, R.W., Shipton, Z.K., Wibberley, C.A.J.,

1049   Withjack, M.O., 2010. A review of recent developments concerning the structure, mechanics

1050   and fluid flow properties of fault zones. Journal of Structural Geology 32, 1557–1575.

1051   https://doi.org/10.1016/j.jsg.2010.06.009

1052   Faulkner, D.R., Mitchell, T.M., Healy, D., Heap, M.J., 2006. Slip on "weak" faults by the rotation of

1053   regional   stress   in   the   fracture   damage   zone.   Nature   444,   922–925.

1054   https://doi.org/10.1038/nature05353

1055   Faulkner, D.R., Rutter, E.H., 1998. The gas permeability of clay-bearing fault gouge at 20 degrees C.

1056   147, 147–156.

1057   Filomena, C.M., Hornung, J., Stollhofen, H., 2014. Assessing accuracy of gas-driven permeability

1058   measurements: A comparative study of diverse Hassler-cell and probe permeameter devices.

1059   Solid Earth 5, 1–11. https://doi.org/10.5194/se-5-1-2014

1060   Forbes Inskip, N.D., Browning, J., Meredith, P.G., Gudmundsson, A., 2020. Conditions for fracture

1061   arrest in layered rock sequences. Results in Geophysical Sciences 1–4, 100001.

1062   https://doi.org/10.1016/j.ringps.2020.100001

1063   Forster, C.B., Evans, J.P., 1991. Hydrogeology of thrust faults and crystalline thrust sheets: results of

1064   combined field and modeling studies. 18, 979–982.

1065   Fossen, H., Hurich, C.A., 2005. The Hardangerfjord Shear Zone in SW Norway and the North Sea:

1066   A large-scale low-angle shear zone in the Caledonian crust. Journal of the Geological Society

1067   162, 675–687. https://doi.org/10.1144/0016-764904-136

1068   Fossen, H., Schultz, R.A., Torabi, A., 2011. Conditions and implications for compaction band

1069   formation in the Navajo Sandstone, Utah. Journal of Structural Geology 33, 1477–1490.

1070   https://doi.org/10.1016/j.jsg.2011.08.001

1071   Fredin, O., Viola, G., Zwingmann, H., Sorlie, R., Bronner, M., Lie, J.E., Grandal, E.M., Muller, A.,

1072   Margreth, A., Vogt, C., Knies, J., 2017a. Correspondence: Reply to Challenges with dating

1073   weathering products to unravel ancient landscapes. Nature Communications 8, 1–2.

1074   https://doi.org/10.1038/s41467-017-01468-6

1075   Fredin, O., Viola, G., Zwingmann, H., Sørlie, R., Brönner, M., Lie, J.E., Grandal, E.M., Müller, A.,

1076   Margreth, A., Vogt, C., Knies, J., 2017b. The inheritance of a mesozoic landscape in western

1077   Scandinavia. Nature Communications 8. https://doi.org/10.1038/ncomms14879

1078   Gabrielsen, R.H., Braathen, A., 2014. Models of fracture lineaments - Joint swarms, fracture corridors

1079   and faults in crystalline rocks, and their genetic relations. Tectonophysics 628, 26–44.

1080   https://doi.org/10.1016/j.tecto.2014.04.022

1081   Gabrielsen, R.H., Kyrkjebø, R., Faleide, J.I., Fjeldskaar, W., Kjennerud, T., 2001. The Cretaceous

1082   post-rift basin configuration of the northern North Sea. Petroleum Geoscience.

1083   https://doi.org/10.1144/petgeo.7.2.137

1084   Gee, D.G., Fossen, H., Henriksen, N., Higgins, A.K., 2008. From the early Paleozoic platforms of

1085   Baltica and Laurentia to the Caledonide Orogen of Scandinavia and Greenland. Episodes 31,

1086   44–51. https://doi.org/10.18814/epiiugs/2008/v31i1/007

1087   Géraud, Y., Rosener, M., Surma, F., Place, J., Le Garzic, É., Diraison, M., 2010. Physical properties

1088   of fault zones within a granite body: Example of the Soultz-sous-Forêts geothermal site.

1089   Comptes Rendus - Geoscience 342, 566–574. https://doi.org/10.1016/j.crte.2010.02.002

1090   Gomila, R., Arancibia, G., Mitchell, T.M., Cembrano, J.M., Faulkner, D.R., 2016. Palaeopermeability

1091   structure within fault-damage zones: A snap-shot from microfracture analyses in a strike-slip

1092   system. Journal of Structural Geology 83, 103–120. https://doi.org/10.1016/j.jsg.2015.12.002

1093   Goodfellow, B.W., Hilley, G.E., Webb, S.M., Sklar, L.S., Moon, S., Olson, C.A., 2016. The chemical,

1094   mechanical, and hydrological evolution of weathering granitoid. Journal of Geohpysical

1095   Research: Earth Surface 1–26. https://doi.org/10.1002/2016JF003822.Received

1096   Gudmundsson, A., Simmenes, T.H., Larsen, B., Philipp, S.L., 2010. Effects of internal structure and

1097   local stresses on fracture propagation, deflection, and arrest in fault zones. Journal of Structural

1098   Geology 32, 1643–1655. https://doi.org/10.1016/j.jsg.2009.08.013

1099   Hayes, J.L., Riebe, C.S., Steven Holbrook, W., Flinchum, B.A., Hartsough, P.C., 2019. Porosity

1100   production in weathered rock: Where volumetric strain dominates over chemical mass loss.

1101   Science Advances 5, 1–12. https://doi.org/10.1126/sciadv.aao0834

1102   Healy, D., 2008. Damage patterns, stress rotations and pore fluid pressures in strike-slip fault zones.

1103   Journal of Geophysical Research: Solid Earth 113, 1–16. https://doi.org/10.1029/2008JB005655

1104   Healy, D., Rizzo, R.E., Cornwell, D.G., Farrell, N.J.C., Watkins, H., Timms, N.E., Gomez-Rivas, E.,

1105   Smith, M., 2017. FracPaQ: A MATLAB^{TM} toolbox for the quantification of fracture patterns.

1106   Journal of Structural Geology 95, 1–16. https://doi.org/10.1016/j.jsg.2016.12.003

1107   Høien, A.H., Nilsen, B., Olsson, R., 2019. Main aspects of deformation and rock support in

1108   Norwegian road tunnels. Tunnelling and Underground Space Technology 86, 262–278.

1109   https://doi.org/10.1016/j.tust.2019.01.026

1110   Holdsworth, R.E., McCaffrey, K.J.W., Dempsey, E., Roberts, N.M.W., Hardman, K., Morton, A.,

1111   Feely, M., Hunt, J., Conway, A., Robertson, A., 2019. Natural fracture propping and earthquake-

1112   induced oil migration in fractured basement reservoirs. Geology 47, 700–704.

1113   https://doi.org/10.1130/G46280.1

1114   Holdsworth, R.E., Trice, R., Hardman, K., McCaffrey, K.J.W., Morton, A., Frei, D., Dempsey, E.,

1115   Bird, A., Rogers, S., 2020. The nature and age of basement host rocks and fissure fills in the

1116   Lancaster field fractured reservoir, West of Shetland. Journal of the Geological Society jgs2019-

1117   142. https://doi.org/10.1144/jgs2019-142

1118   Howell, J.A., Martinius, A.W., Good, T.R., 2014. The application of outcrop analogues in geological

1119   modelling: a review, present status and future outlook. Geological Society, London, Special

1120   Publications 387, 1–25. https://doi.org/10.1144/sp387.12

1121   Jeanne, P., Guglielmi, Y., Cappa, F., 2013. Hydromechanical heterogeneities of a mature fault zone:

1122   Impacts on fluid flow. Groundwater 51, 880–892. https://doi.org/10.1111/gwat.12017

1123   Jeanne, P., Guglielmi, Y., Rutqvist, J., Nussbaum, C., Birkholzer, J., 2017. Field characterization of

1124   elastic properties across a fault zone reactivated by fluid injection. Journal of Geophysical

1125   Research: Solid Earth 122, 6583–6598. https://doi.org/10.1002/2017JB014384

1126   Jones, R.R., McCaffrey, K.J.W., Imber, J., Wightman, R., Smith, S.A.F., Holdsworth, R.E., Clegg,

1127   P., De Paola, N., Healy, D., Wilson, R.W., 2008. Calibration and validation of reservoir models:

1128   The importance of high resolution, quantitative outcrop analogues. Geological Society Special

1129   Publication 309, 87–98. https://doi.org/10.1144/SP309.7

1130   Kitchka, A.A., Petrovskyy, O.P., Fedchenko, T.O., Kuzmanenko, G.O., Solomyanyi, A.R., 2017.

1131   Analogue Outcrops Study of the Weathered Crystalline Crust Benefits for Basement Reservoirs

1132   Exploration in Ukraine. European Association of Geoscientists & Engineers, 1–5.

1133   https://doi.org/10.3997/2214-4609.201700881

1134 Koning, T., 2003. Oil and gas production from basement reservoirs: Examples from Indonesia, USA

1135   and Venezuela. Geological Society Special Publication.

1136   https://doi.org/10.1144/GSL.SP.2003.214.01.05

1137 Leclère, H., Cappa, F., Faulkner, D.R., Fabbri, O., Armitage, P., Blake, O., 2015. Development and

1138   maintenance of fluid overpressures in crustal fault zones by elastic compaction and implications

1139   for earthquake swarms. Journal of Geophysical Research: Solid Earth 120, 4450–4473.

1140   https://doi.org/10.1002/2014JB011759

1141 Long, J.C.S., Remer, J.S., Wilson, C.R., Witherspoon, P.A., 1982. Porous media equivalents for

1142   networks of discontinuous fractures. Water Resources Research 18, 645–658.

1143   https://doi.org/10.1029/WR018i003p00645

1144 Lothe, A.E., Emmel, B., Bergmo, P.E., Akervoll, I., Todorovic, J., Bhuiyan, M.H., Knies, J., 2018.

1145   Porosity, permeability and compaction trends for Scandinavian regoliths. Marine and Petroleum

1146   Geology 92, 319–331. https://doi.org/10.1016/j.marpetgeo.2017.10.027

1147 Lundmark, A.M., Sæther, T., Sørlie, R., 2014. Ordovician to silurian magmatism on the Utsira High,

1148   North Sea: Implications for correlations between the onshore and offshore Caledonides.

1149   Geological Society Special Publication 390, 513–523. https://doi.org/10.1144/SP390.21

1150 Luthi, S.M., 2005. Fractured reservoir analysis using modern geophysical well techniques:

1151   Application to basement reservoirs in Vietnam. Geological Society Special Publication 240, 95–

1152   106. https://doi.org/10.1144/GSL.SP.2005.240.01.08

1153 McCaffrey, K.J.W., Holdsworth, R.E., Pless, J., Franklin, B.S.G., Hardman, K., 2020. Basement

1154   reservoir plumbing: fracture aperture, length and topology analysis of the Lewisian Complex,

1155   NW   Scotland.   Journal   of   the   Geological   Society.

1156   https://doi.org/https://doi.org/10.1144/jgs2019-143 This

1157   Migoń, P., Thomas, M.F., 2002. Grus weathering mantles - Problems of interpretation. Catena 49, 5–

1158   24. https://doi.org/10.1016/S0341-8162(02)00014-0

1159   Mitchell, T.M., Faulkner, D.R., 2012. Towards quantifying the matrix permeability of fault damage

1160   zones in low porosity rocks. Earth and Planetary Science Letters 339–340, 24–31.

1161   https://doi.org/10.1016/j.epsl.2012.05.014

1162   Niemeijer, A.R., Spiers, C.J., 2005. Influence of phyllosilicates on fault strength in the brittle-ductile

1163   transition: Insights from rock analogue experiments. Geological Society Special Publication

1164   245, 303–327. https://doi.org/10.1144/GSL.SP.2005.245.01.15

1165   Ortega, O.J., Marrett, R.A., Laubach, S.E., 2006. A scale-independent approach to fracture intensity

1166   and average spacing measurement. American Association of Petroleum Geologists Bulletin 90,

1167   193–208. https://doi.org/10.1306/08250505059

1168   Place, J., Géraud, Y., Diraison, M., Herquel, G., Edel, J.B., Bano, M., Le Garzic, E., Walter, B., 2016.

1169   Structural control of weathering processes within exhumed granitoids: Compartmentalisation of

1170   geophysical properties by faults and fractures. Journal of Structural Geology 84, 102–119.

1171   https://doi.org/10.1016/j.jsg.2015.11.011

1172   Primaleon, L.P., McCaffrey, K.J.W., Holdsworth, R.E., 2020. Fracture attribute and topology

1173   characteristics of a geothermal reservoir: Southern Negros, Philippines. Journal of the

1174   Geological Society 177, 1092 LP – 1106. https://doi.org/10.1144/jgs2019-126

1175   Rempe, M., Mitchell, T.M., Renner, J., Smith, S.A.F., Bistacchi, A., Di Toro, G., 2018. The

1176   Relationship Between Microfracture Damage and the Physical Properties of Fault-Related

1177   Rocks: The Gole Larghe Fault Zone, Italian Southern Alps. Journal of Geophysical Research:

1178   Solid Earth 123, 7661–7687. https://doi.org/10.1029/2018JB015900

1179   Riber, L., Driese, S.G., Stinchcomb, G.E., Dypvik, H., Sørlie, R., 2019a. Reconstructing a high

1180   paleolatitude Mesozoic paleoenvironment from a truncated and deeply buried regolith,

1181   Norwegian North Sea. Palaeogeography, Palaeoclimatology, Palaeoecology 528, 60–77.

1182   https://doi.org/10.1016/J.PALAEO.2019.04.031

1183   Riber, L., Driese, S.G., Stinchcomb, G.E., Dypvik, H., Sørlie, R., 2019b. Reconstructing a high

1184   paleolatitude Mesozoic paleoenvironment from a truncated and deeply buried regolith,

1185   Norwegian North Sea. Palaeogeography, Palaeoclimatology, Palaeoecology 528, 60–77.

1186   https://doi.org/10.1016/j.palaeo.2019.04.031

1187   Riber, L., Dypvik, H., Sørlie, R., 2015. Altered basement rocks on the Utsira High and its

1188   surroundings, Norwegian North Sea. Norwegian Journal of Geology 95, 57–89.

1189   https://doi.org/10.17850/njg95-1-04

1190   Riber, L., Dypvik, H., Sørlie, R., Ferrell, R.E., 2016. Clay minerals in deeply buried paleoregolith

1191   profiles, Norwegian North Sea. Clays and Clay Minerals 64, 588–607.

1192   https://doi.org/10.1346/CCMN.2016.064036

1193   Riber, L., Dypvik, H., Sørlie, R., Naqvi, S.A.A.E.M., Stangvik, K., Oberhardt, N., Schroeder, P.A.,

1194   2017. Comparison of deeply buried paleoregolith profiles, Norwegian North Sea, with outcrops

1195   from southern Sweden and Georgia, USA — Implications for petroleum exploration.

1196   Palaeogeography, Palaeoclimatology, Palaeoecology 471, 82–95.

1197   https://doi.org/10.1016/j.palaeo.2017.01.043

1198   Roberts, D., 2003. The Scandinavian Caledonides: Event chronology, palaeogeographic settings and

1199   likely modern analogues. Tectonophysics 365, 283–299. https://doi.org/10.1016/S0040-

1200   1951(03)00026-X

1201   Rutqvist, J., Stephansson, O., 2003. The role of hydrochemical coupling in fractured rock

1202   engineering. Hydrogeology Journal 11, 7–40. https://doi.org/10.1007/s10040-002-0241-5

1203   Ryan, R.J., O'Beirne-Ryan, A.M., Zentilli, M., 2005. Rounded cobbles that have not travelled far:

1204   Incorporation of corestones from saprolites in the South Mountain area of southern Nova Scotia,

1205   Canada. Sedimentology 52, 1109–1121. https://doi.org/10.1111/j.1365-3091.2005.00730.x

1206   Scheiber, T., Viola, G., 2018. Complex Bedrock Fracture Patterns: A Multipronged Approach to

1207   Resolve Their Evolution in Space and Time. Tectonics 37, 1030–1062.

1208   https://doi.org/10.1002/2017TC004763

1209   Scheiber, T., Viola, G., Wilkinson, C.M., Ganerød, M., Skår, Ø., Gasser, D., 2016. Direct40Ar/39Ar

1210   dating of Late Ordovician and Silurian brittle faulting in the southwestern Norwegian

1211   Caledonides. Terra Nova 28, 374–382. https://doi.org/10.1111/ter.12230

1212   Scibek, J., 2020. Multidisciplinary database of permeability of fault zones and surrounding protolith

1213   rocks at world-wide sites. Scientific Data 7, 1–14. https://doi.org/10.1038/s41597-020-0435-5

1214   Sclater, J.G., Christie, P.A.F., 1980. Continental stretching: An explanation of the Post-Mid-

1215   Cretaceous subsidence of the central North Sea Basin. Journal of Geophysical Research: Solid

1216   Earth. https://doi.org/10.1029/jb085ib07p03711

1217   Shea, W.T., Kronenberg, A.K., 1993. Strength and anisotropy of foliated rocks with varied mica

1218   contents. Journal of Structural Geology 15, 1097–1121. https://doi.org/10.1016/0191-

1219   8141(93)90158-7

1220   Sibson, R.H., Rowland, J. V., 2003. Stress, fluid pressure and structural permeability in seismogenic

1221   crust, North Island, New Zealand. Geophysical Journal International 154, 584–594.

1222   https://doi.org/10.1046/j.1365-246X.2003.01965.x

1223   Slagstad, T., Davidsen, B., Stephen Daly, J., 2011. Age and composition of crystalline basement rocks

1224   on the norwegian continental margin: Offshore extension and continuity of the Caledonian-

1225   Appalachian orogenic belt. Journal of the Geological Society 168, 1167–1185.

1226   https://doi.org/10.1144/0016-76492010-136

1227   Smart, K.J., Ofoegbu, G.I., Morris, A.P., McGinnis, R.N., Ferrill, D.A., 2014. Geomechanical

1228   modeling of hydraulic fracturing: Why mechanical stratigraphy, stress state, and pre-existing

1229   structure matter. AAPG Bulletin 98, 2237–2261. https://doi.org/10.1306/07071413118

1230   Souque, C., Knipe, R.J., Davies, R.K., Jones, P., Welch, M.J., Lorenz, J., 2019. Fracture corridors

1231   and fault reactivation: Example from the Chalk, Isle of Thanet, Kent, England. Journal of

1232   Structural Geology 122, 11–26. https://doi.org/10.1016/j.jsg.2018.12.004

1233   Staněk, M., Géraud, Y., 2019. Granite microporosity changes due to fracturing and alteration:

1234   Secondary mineral phases as proxies for porosity and permeability estimation. Solid Earth 10,

1235   251–274. https://doi.org/10.5194/se-10-251-2019

1236   Steefel, C.I., Mäher, K., 2009. Fluid-rock interaction: A reactive transport approach. Reviews in

1237   Mineralogy and Geochemistry 70, 485–532. https://doi.org/10.2138/rmg.2009.70.11

1238   Steer, P., Bigot, A., Cattin, R., Soliva, R., 2011. In-situ characterization of the effective elasticity of

1239   a fault zone, and its relationship to fracture spacing. Journal of Structural Geology 33, 1541–

1240   1553. https://doi.org/10.1016/j.jsg.2011.09.009

1241   Stober, I., Bucher, K., 2015. Hydraulic conductivity of fractured upper crust: Insights from hydraulic

1242   tests in boreholes and fluid-rock interaction in crystalline basement rocks. Geofluids 15, 161–

1243   178. https://doi.org/10.1111/gfl.12104

1244   Stober, I., Bucher, K., 2007. Hydraulic properties of the crystalline basement. Hydrogeology Journal

1245   15, 213–224. https://doi.org/10.1007/s10040-006-0094-4

1246   Tanner, D.C., Buness, H., Igel, J., Günther, T., Gabriel, G., Skiba, P., Plenefisch, T., Gestermann, N.,

1247   Walter, T.R., 2019. Fault detection, Understanding Faults: Detecting, Dating, and Modeling.

1248   https://doi.org/10.1016/B978-0-12-815985-9.00003-5

1249   Tartaglia, G., Viola, G., van der Lelij, R., Scheiber, T., Ceccato, A., Schönenberger, J., 2020. "Brittle

1250   structural facies" analysis: A diagnostic method to unravel and date multiple slip events of long-
1251   lived faults. Earth and Planetary Science Letters 545, 116420.
1252   https://doi.org/10.1016/j.epsl.2020.116420

1253   Torabi, A., Alaei, B., Ellingsen, T.S.S., 2018. Faults and fractures in basement rocks, their
1254   architecture, petrophysical and mechanical properties. Journal of Structural Geology 117, 256–
1255   263. https://doi.org/10.1016/j.jsg.2018.07.001

1256   Torabi, A., Berg, S.S., 2011. Scaling of fault attributes: A review. Marine and Petroleum Geology
1257   28, 1444–1460. https://doi.org/10.1016/j.marpetgeo.2011.04.003

1258   Trice, R., Hiorth, C., Holdsworth, R., 2019. Fractured basement play development on the UK and
1259   Norwegian rifted margins. Geological Society, London, Special Publications SP495-2018–174.
1260   https://doi.org/10.1144/sp495-2018-174

1261   van Noort, R., Yarushina, V., 2019. Water, CO_2 and Argon Permeabilities of Intact and Fractured
1262   Shale Cores Under Stress. Rock Mechanics and Rock Engineering 52, 299–319.
1263   https://doi.org/10.1007/s00603-018-1609-8

1264   Vignaroli, G., Giallini, S., Polpetta, F., Sirianni, P., Gaudiosi, I., Simionato, M., Razzano, R.,
1265   Pagliaroli, A., Moscatelli, M., Mancini, M., Cavinato, G.P., Avalle, A., 2019. Domains of
1266   seismic noise response in faulted limestone (central Apennines, Italy): insights into fault-related
1267   site effects and seismic hazard. Bulletin of Engineering Geology and the Environment 78, 2749–
1268   2768. https://doi.org/10.1007/s10064-018-1276-8

1269   Viola, G., Scheiber, T., Fredin, O., Zwingmann, H., Margreth, A., Knies, J., 2016. Deconvoluting
1270   complex structural histories archived in brittle fault zones. Nature Communications 7, 1–10.
1271   https://doi.org/10.1038/ncomms13448

1272   Walsh, J.J., Watterson, J., Bailey, W.R., Childs, C., 1999. Fault relays, bends and branch-lines.
1273   Journal of Structural Geology. https://doi.org/10.1016/S0191-8141(99)00026-7

1274   Walsh, J.J., Watterson, J., Heath, A., Gillespie, P.A., Childs, C., 1998. Assessment of the effects of

1275   sub-seismic faults on bulk permeabilities of reservoir sequences. Geological Society Special

1276   Publication 127, 99–114. https://doi.org/10.1144/GSL.SP.1998.127.01.08

1277   Walter, B., Géraud, Y., Bartier, D., Kluska, J.M., Diraison, M., Morlot, C., Raisson, F., 2018.

1278   Petrophysical and mineralogical evolution of weathered crystalline basement in western

1279   Uganda: Implications for fluid transfer and storage. AAPG Bulletin 102, 1035–1065.

1280   https://doi.org/10.1306/0810171610917171

1281   Watkins, H., Bond, C.E., Healy, D., Butler, R.W.H., 2015. Appraisal of fracture sampling methods

1282   and a new workflow tocharacterise heterogeneous fracture networks at outcrop. Journal of

1283   Structural Geology 72, 67–82. https://doi.org/10.1016/j.jsg.2015.02.001

1284   Watkins, H., Healy, D., Bond, C.E., Butler, R.W.H., 2018. Implications of heterogeneous fracture

1285   distribution on reservoir quality; an analogue from the Torridon Group sandstone, Moine Thrust

1286   Belt, NW Scotland. Journal of Structural Geology 108, 180–197.

1287   https://doi.org/10.1016/j.jsg.2017.06.002

1288   Wibberley, C.A.J., Yielding, G., Di Toro, G., 2008. Recent advances in the understanding of fault

1289   zone internal structure: A review. Geological Society Special Publication 299, 5–33.

1290   https://doi.org/10.1144/SP299.2

1291   Wilson, J.E., Chester, J.S., Chester, F.M., 2003. Microfracture analysis of fault growth and wear

1292   processes, Punchbowl Fault, San Andreas system, California. Journal of Structural Geology 25,

1293   1855–1873. https://doi.org/10.1016/S0191-8141(03)00036-1

1294   Zauyah, S., Schaefer, C.E.G.R., Simas, F.N.B., 2018. Chapter 3 Saprolites, Interpretation of

1295   Micromorphological Features of Soils and Regoliths. Elsevier B.V.

1296   https://doi.org/10.1016/B978-0-444-63522-8.00003-6

1297   Zhang, S., Tullis, T.E., 1998. The effect of fault slip on permeability and permeability anisotropy in

1298 quartz gouge. Tectonophysics 295, 41–52. https://doi.org/10.1016/S0040-1951(98)00114-0

1299